Self-dynamics of hydrogen gas as probed by means of inelastic neutron scattering

2005 J. Phys.: Condens. Matter 17 7895

(http://iopscience.iop.org/0953-8984/17/50/010)

INSTITUTE OF PHYSICS PUBLISHING JOURNAL OF PHYSICS: CONDENSED MATTER

J. Phys.: Condens. Matter **17** (2005) 7895–7923 doi:10.1088/0953-8984/17/50/010

Self-dynamics of hydrogen gas as probed by means of inelastic neutron scattering

Eleonora Guarini[1], Andrea Orecchini[2], Ferdinando Formisano[3], Franz Demmel[4,6], Caterina Petrillo[2], Francesco Sacchetti[2], Ubaldo Bafile[5] and Fabrizio Barocchi[1]

[1] CNR-INFM and CRS-Soft, c/o Dipartimento di Fisica, Università di Firenze, via G Sansone 1, I-50019 Sesto Fiorentino, Italy
[2] Dipartimento di Fisica and CRS-Soft, Università di Perugia, via A Pascoli, I-06100 Perugia, Italy
[3] CNR-INFM OGG and CRS-Soft, c/o Institut Laue-Langevin, 6 rue J. Horowitz, BP 156, F-38042 Grenoble, France
[4] Institut Laue Langevin, 6 rue J. Horowitz, BP 156, F-38042 Grenoble, France
[5] Istituto dei Sistemi Complessi CNR Firenze, via Madonna del Piano, I-50019 Sesto Fiorentino, Italy

Received 1 July 2005, in final form 4 November 2005
Published 2 December 2005
Online at stacks.iop.org/JPhysCM/17/7895

Abstract

The neutron double-differential cross-section of molecular hydrogen at low density has been measured at two rather low scattering angles and different final neutron energies by means of three-axis spectrometry. This first inelastic scattering determination of the single-particle roto-translational dynamics of room temperature H_2 allows for a detailed test of the theoretical modelling of the spectral line-shapes of such a fundamental molecule, performed by referring both to a careful quantum-mechanical treatment and to a simpler semi-classical approximation. A comprehensive report on the neutron measurements and data analysis is presented, along with an overview of the theories used for comparison with the experimental results. An encouraging picture of the present capabilities in the calculation of the true dynamic response of hydrogen gas to slow and thermal neutrons is obtained, opening new perspectives for accurate data calibration in inelastic neutron spectroscopy, with special relevance for small-angle experiments.

1. Introduction

Neutrons provide the rare possibility of probing directly the single-particle dynamic properties of fluids over a wide kinematic range, extending from the hydrodynamic regime (self-diffusion) to the kinetic one (free motion) [1]. This special capability originates from the double nature, *coherent* and *incoherent*, of the neutron scattering length for each isotope in the

[6] Present address: ISIS Facility, Rutherford Appleton Laboratory, Chilton, Oxfordshire OX11 0QX, UK.

periodic system [2]. Atoms and molecules with predominantly incoherent neutron cross-sections constitute ideal samples for self-dynamics investigations by neutron spectroscopy. Indeed, the incoherent neutron scattering, as a function of the momentum $\hbar Q$ and energy $\hbar\omega$ exchanged between the probe and the sample, gives direct access to the self-dynamic structure factor $S_{\rm self}(Q,\omega)$, i.e. the sought-for quantity when single-particle properties are addressed. Conversely, other spectroscopic techniques, including coherent neutron scattering, can only determine the total dynamic structure factor $S(Q,\omega)$, which, being related to the sum of distinct-particle and single-particle space and time correlations, gives information on the collective dynamics.

Hydrogen is a strongly incoherent neutron scatterer. In this respect, all hydrogen-containing compounds are ideal systems for self-dynamics studies, as proved for example by the increasing applications of the incoherent neutron scattering technique to biological systems, where the abundance of H atoms allows an efficient study of the close connection between molecular dynamics and biological functionality. As regards pure molecular hydrogen, many studies have been devoted, from the early 1940s to current times, to the theoretical modelling of the dynamic response to neutrons of this system [2–15], which is fundamental not only from a scientific point of view, but also for applications in neutron technology, hydrogen being an efficient moderator and cold neutron source at liquid densities. The case of hydrogen is however partly anomalous with respect to those of other important simple molecular fluids such as methane, since the considerable amount of theoretical work was not equally supported by inelastic neutron scattering experiments. Indeed, existing dynamical measurements have been concentrated on the liquid and dense gaseous phases, concerning in particular deep inelastic neutron scattering (DINS) for mean kinetic energy and momentum distribution determinations in the impulse approximation [16–20]. However, most models for the neutron double-differential cross-section of H_2 [2–14], including the detailed quantum-mechanical description proposed by Young and Koppel (YK) [8, 9], are based on the typical assumption of ideal gas behaviour for the translational dynamics, and on other basic approximations, like the neglect of intramolecular roto-vibrational coupling, and the assumption of harmonic vibrations. Thus, available models have been developed to be a good approximation, generally, in the dilute phase and below the epithermal energies typical of DINS, which, while allowing for the free-translation hypothesis even for a dense liquid, prevent testing the above original schemes because of the anharmonicity of vibrations and roto-vibrational coupling induced by the incident neutrons.

To our knowledge, the only case in which a hydrogen model (YK) has been compared with inelastic scattering data collected in more appropriate conditions for model testing is the one reported by Herwig and Simmons [21], where measurements on cold (18 K) hydrogen vapour in equilibrium with the liquid were performed by using a fixed incident energy of 504 meV and scattering angles above 18°. There, however, only the relative intensities of individual rotational lines contributing to the spectrum were derived through a fit to the data and compared with the corresponding YK predictions; thus only indirect, and somewhat approximate, indications of the ability of the model to reproduce the total experimental spectrum of hydrogen were obtained. Moreover, (i) due to the low temperature, only few rotational levels were thermally populated; and (ii) the low-energy, low-angle part of the kinematic range, which is quite interesting for the reasons explained below, was not probed in that experiment.

Therefore, calculations of the dynamic cross-section of hydrogen have never been thoroughly tested against inelastic measurements performed in the ideal conditions for which most models have been developed, i.e. in the low-density room temperature gaseous phase and well below the extreme kinematic conditions of DINS. Only indirect (integral) tests have

been performed in past years for room temperature hydrogen by comparison of calculations with total neutron cross-section data [22], and with differential cross-section results ($d\sigma/d\Omega$) obtained by slow-neutron diffraction on dilute H_2 [13]. As a matter of fact, we neither know how the accuracy of the proposed dynamical models varies with decreasing neutron energy and scattering angle nor have indications about their reliability when several rotational transitions contribute not only to the (neutron) energy-loss part, but also to the energy-gain part of the spectrum. Without this basic knowledge, it is also impossible to evaluate the efficacy of related 'modified' models later introduced for the double-differential cross-section in more complex cases, like those of applicative interest concerning low-temperature liquid hydrogen and its dynamic response to high-energy neutrons (e.g. above 0.5 eV). For instance, in these latter cases corrections of the original schemes were reasonably introduced to account for centrifugal distortion, anharmonicity of vibrations and quantum effects [16] making the mean translational kinetic energy differ from the classical value of $\frac{3}{2}k_{\mathrm{B}}T$, or, finally, to improve the description of the translational dynamics for a dense liquid [14, 23], which, except in the impulse approximation, greatly differs from the ideal gas one assumed in all the earlier theoretical works [4–10]. It is worth noting that later improvements and modifications have often been applied to essentially *one* original model, i.e. the quantum YK one. However, since this model still requires a detailed experimental verification in its original form, it is even more the case that no real conclusion can be drawn, in principle, about the accuracy of its extensions and modifications.

Here we present the results of an inelastic scattering determination of the self-dynamic cross-section of dilute room temperature H_2, at two different final neutron energies, namely 14.68 and 50 meV. The present capabilities in the *ab initio* calculation of the hydrogen neutron spectra, including a detailed quantum treatment of the roto-vibrational single-molecule dynamics, are probed over a rather extended energy transfer range, where different sets of rotational transitions can be activated by the incident neutrons. In particular, the calculations are tested against experiment both below and above the threshold energy (14.7 meV) for activation of the first rotational transition in hydrogen, since variable incident neutron energies were used in the measurements (see the experimental details in section 4), from rather low values such as 10.7 meV, up to 59.5 meV. Moreover, rather low scattering angles, 2° and 7°, were investigated to enable an experimental verification of the calculations in the most demanding conditions, i.e. where the ideal gas law, used to model the translations of the molecules, foresees a steep decrease of the width of the translational spectrum [14]. The case of scattering angles below 30° is, for instance, the one giving rise to the most evident differences between experimental data and model calculations of the neutron double-differential cross-section of gaseous methane [2, 13, 24–26], and represents a stringent test to be performed for hydrogen as well.

Producing first experimental results for the neutron inelastic spectra of gaseous hydrogen at room temperature, and comparing them with available, refined theoretical descriptions, has indeed a fundamental interest. It is important, however, to note that, if data and calculations agree at a high level of accuracy, one obtains a tested and valuable method for inelastic scattering data normalization, using hydrogen as a *reference sample* for deriving the conversion factor between experimental (arbitrary) and absolute units for any other sample measured with the same instrumental set-up. In this respect, encouraging results have been obtained, though at the less demanding level of integrated spectra, in the normalization of differential cross-section data obtained by means of neutron diffraction [13, 27].

In order to evaluate the importance of using room temperature H_2 gas for normalization purposes, it should be borne in mind that:

(i) The widespread use of vanadium as a neutron reference sample may sometimes become rather problematic and imprecise, due to the increasing and unpredictable spurious signal

from this sample as smaller and smaller Q values are approached, which is generally due to impurities and residual stresses induced by manufacturing.

(ii) The availability of a gaseous standard is an important advantage in experiments on fluids, since identical sample–container geometries can generally be maintained in all measurements, both for the system under study and the reference sample, thus allowing for a more accurate data reduction to absolute units.

(iii) The use of room temperature makes the hydrogen sample preparation extremely easy, with little ancillary equipment required and low gas consumption.

(iv) In comparison with dilute CH_4 [28], another predominantly incoherent neutron scatterer for which quantum-mechanical models of the self-double-differential cross-section have been developed and refined during recent years [13, 26], hydrogen has the advantage that thermal and hot neutrons excite far fewer rotational transitions and no vibrational ones, so models and numerical calculations are more easily, and to a better accuracy, implemented.

Moreover, the above-mentioned difficulties in reproducing with accuracy the CH_4 neutron spectra at scattering angles below 30° make methane unsuited, at least with the present modelling tools, for normalization at low angles and, consequently, for avoiding the low-Q inaccuracies found with vanadium. Thus, the hydrogen method, although of general application irrespectively of the type and geometry of the neutron spectrometer used, would be particularly valuable for small-angle inelastic instruments, like the novel neutron Brillouin spectrometer BRISP at the Institut Laue-Langevin in Grenoble [29].

We stress, however, that the foreseen use of hydrogen as a calibration standard can only be proposed after having demonstrated that the available methods for calculating H_2 inelastic neutron spectra enable a good description of the experimental results. It is the purpose of this work to show that such is indeed the case, provided that the quantum nature and contribution to scattering of individual rotational states are duly taken into account, as is done by the YK model. We will also show that a simpler quasi-classical treatment such as the one proposed by Krieger and Nelkin (KN) [7], though able to approximately account for the observed dynamics, cannot fully reproduce, as partly expected from its intrinsic limitations, slow-neutron and thermal neutron experimental spectra over energy transfer domains as important as the elastic and quasi-elastic ones.

The contents of this paper are organized as follows. Sections 2 and 3 summarize the theoretical background by reporting, respectively, basic relations for neutron scattering and the main features of the models adopted for the description of the hydrogen neutron spectra. In section 4 the experiment is described in some detail, while section 5 is devoted to data treatment. The results and conclusions of this investigation are finally discussed in section 6.

2. Basic theory

In the following we first refer to the simpler case of monatomic samples in order to allow for a smoother understanding of the fundamental concepts at the basis of neutron inelastic scattering investigations of fluid dynamics. These concepts will then be extended to the case of molecular systems in the next section.

The dynamical quantity accessed by inelastic neutron scattering on a monatomic sample composed of N nuclei with time-dependent position vectors $\boldsymbol{R}_1(t) \ldots \boldsymbol{R}_N(t)$ is the double-differential cross-section per unit solid angle and unit frequency interval [2]:

$$\frac{\mathrm{d}^2\sigma}{\mathrm{d}\Omega\,\mathrm{d}\omega} = \frac{k_1}{k_0}\frac{1}{2\pi}\int \mathrm{d}t\,\mathrm{e}^{-\mathrm{i}\omega t}\frac{1}{N}\sum_{\alpha,\beta=1}^{N}\langle b_\alpha^*\mathrm{e}^{-\mathrm{i}\boldsymbol{Q}\cdot\boldsymbol{R}_\alpha(0)}b_\beta\mathrm{e}^{\mathrm{i}\boldsymbol{Q}\cdot\boldsymbol{R}_\beta(t)}\rangle = \frac{k_1}{k_0}\tilde{S}(Q,\omega), \tag{1}$$

which is proportional to the probability per unit time of any energy-conserving scattering process where the neutron wavevector undergoes the transition $\boldsymbol{k}_0 \rightarrow \boldsymbol{k}_1$, corresponding to a momentum transfer $\hbar\boldsymbol{Q} = \hbar(\boldsymbol{k}_0 - \boldsymbol{k}_1)$. In equation (1), the fingerprints of the probe that we are using for the investigation of the system dynamics are represented by the ratio k_1/k_0 of the final and incident neutron wavevectors, and by the nuclear neutron scattering lengths b_i, which depend on the total spin of the neutron plus ith nucleus system. Further, we indicated the time Fourier transform in equation (1) as $\tilde{S}(Q, \omega)$ in order to underline its close relation with the relevant dynamical quantity in the theory of fluids, i.e. the dynamic structure factor $S(Q, \omega)$. The latter, defined as the time Fourier transform of the intermediate scattering function (ISF) $F(Q, t)$ measuring the global density correlation, in the reciprocal space, between couples of atoms at different times [1, 30], is in fact given by

$$S(Q,\omega) = \frac{1}{2\pi}\int \mathrm{d}t\, \mathrm{e}^{-\mathrm{i}\omega t} F(Q,t) \qquad \text{with } F(Q,t) = \frac{1}{N}\sum_{\alpha,\beta=1}^{N} \langle \mathrm{e}^{-\mathrm{i}\boldsymbol{Q}\cdot\boldsymbol{R}_\alpha(0)} \mathrm{e}^{\mathrm{i}\boldsymbol{Q}\cdot\boldsymbol{R}_\beta(t)} \rangle \tag{2}$$

where we used the explicit expression $\sum_{i=1}^{N} \mathrm{e}^{\mathrm{i}\boldsymbol{Q}\cdot\boldsymbol{R}_i(t)}$ for the space Fourier transform of the time-dependent local density $\rho(\boldsymbol{r}, t) = \sum_{i=1}^{N} \delta(\boldsymbol{r} - \boldsymbol{R}_i(t))$, and the brackets $\langle \cdots \rangle$ indicate the statistical average in the canonical ensemble.

The comparison of equations (1) and (2) shows that $\tilde{S}(Q, \omega)$, as obtained from neutron scattering, would be strictly proportional to the dynamic structure factor $S(Q, \omega)$ if the neutron scattering lengths in equation (1) were identical for all the nuclei in the system. Before deepening this last aspect, it is useful to note that in equation (2) no distinction was made between correlations involving *different* atoms and those relating the position of the *same* atom at different times. If such a distinction is made, it is possible to define *self*-ISF ($\alpha = \beta$) and *distinct* ISF ($\alpha \neq \beta$) [1, 30], $F_\mathrm{s}(Q, t)$ and $F_\mathrm{d}(Q, t)$, and, consequently, analogous contributions to the dynamic structure factor, such that $S(Q, \omega) = S_\mathrm{s}(Q, \omega) + S_\mathrm{d}(Q, \omega)$. Such a separation helps in clarifying the role of coherent and incoherent scattering in determinations of $\tilde{S}(Q, \omega)$ by the neutron technique. Without going into details which can be deepened by referring to the literature on neutron scattering, e.g. [2], whenever the spin variables (contained in the scattering lengths) can be considered as uncorrelated with the nuclear coordinates, it is possible to separate in equation (1) the correlation of the scattering lengths from that of the exponentials. Such a decoupling is justified, in principle, only when dealing with a monoisotopic system and an unpolarized neutron beam. In this case, by introducing the coherent and incoherent neutron scattering lengths, b_coh and b_inc, as the average and spread of the b distribution originating from the variable coupling between the neutron and nuclear spin orientations, and by using the relation $\langle b_\alpha^* b_\beta \rangle = b_\mathrm{coh}^2 + \delta_{\alpha\beta} b_\mathrm{inc}^2$, with $\delta_{\alpha\beta}$ the Kronecker's symbol, it is possible to rewrite $\tilde{S}(Q, \omega)$ in terms of *self*-contributions and *distinct* contributions, as

$$\begin{aligned}\tilde{S}(Q,\omega) &= \frac{1}{2\pi}\int \mathrm{d}t\, \mathrm{e}^{-\mathrm{i}\omega t}[b_\mathrm{coh}^2 F_\mathrm{d}(Q,t) + (b_\mathrm{coh}^2 + b_\mathrm{inc}^2) F_\mathrm{s}(Q,t)] \\ &= b_\mathrm{coh}^2 S_\mathrm{d}(Q,\omega) + (b_\mathrm{coh}^2 + b_\mathrm{inc}^2) S_\mathrm{s}(Q,\omega) \\ &= [\sigma_\mathrm{coh} S_\mathrm{d}(Q,\omega) + (\sigma_\mathrm{coh} + \sigma_\mathrm{inc}) S_\mathrm{s}(Q,\omega)]/4\pi \end{aligned} \tag{3}$$

where we also introduced the coherent and incoherent neutron scattering cross-sections, $\sigma_\mathrm{coh} = 4\pi b_\mathrm{coh}^2$ and $\sigma_\mathrm{inc} = 4\pi b_\mathrm{inc}^2$, typically tabulated in units of barns (1 b $= 10^{-24}$ cm^2) for each isotope of the periodic system. However, even when referring to monatomic samples, one deals, in general, with a collection of various isotopes of the same element, and thus with a collection of different scattering cross-sections. In this case, the values of σ_coh and σ_inc to be used are those taking into account the isotopic composition of the sample and its contribution to the total incoherence. The first formulation given in equation (3) will be useful for the

generalization to molecular systems. As regards the third expression, we note that it can be equivalently written as

$$\tilde{S}(Q,\omega) = \frac{\sigma_{\mathrm{coh}}}{4\pi} S(Q,\omega) + \frac{\sigma_{\mathrm{inc}}}{4\pi} S_{\mathrm{s}}(Q,\omega) \tag{4}$$

which clarifies how, as anticipated in the introduction, coherent neutron scattering probes the total (collective) dynamics and incoherent neutron scattering gives direct access to the single-particle dynamics (self-dynamics). For a very dilute gas, with negligible interparticle interactions, the total dynamic structure factor reduces to the self-part only [2]; thus neutron inelastic scattering allows us to determine

$$\tilde{S}(Q,\omega) = \frac{\sigma_{\mathrm{coh}} + \sigma_{\mathrm{inc}}}{4\pi} S_{\mathrm{s}}(Q,\omega) \tag{5}$$

where $\sigma_{\mathrm{s}} = \sigma_{\mathrm{coh}} + \sigma_{\mathrm{inc}}$ is the total scattering cross-section and $S_{\mathrm{s}}(Q,\omega)$ will be very close to the well-known *ideal gas* (i.g.) scattering law [2]:

$$S_{\mathrm{s}}^{\mathrm{i.g.}}(Q,\omega) = \sqrt{\frac{M}{2\pi k_{\mathrm{B}} T Q^2}} \exp\left[-\frac{M}{2k_{\mathrm{B}} T Q^2} \left(\omega - \frac{\hbar Q^2}{2M} \right)^2 \right], \tag{6}$$

with T the gas temperature and M the atomic mass.

It is finally useful to briefly discuss the connection between experimental intensities collected in a neutron scattering experiment and the sought-for dynamic quantities. Even in idealized conditions, i.e. with negligible neutron absorption by the nuclei and no occurrence of multiple-scattering events in the sample, the measured signal $\mathrm{d}I/\mathrm{d}\omega$ (here taken as the count rate per unit frequency interval) differs from the double-differential cross-section of equation (1) by an instrumental factor that depends on the neutron flux at the sample Φ, the solid angle element $\Delta\Omega$ subtended by the detector, the detector neutron absorption efficiency $\varepsilon(k_1)$ and other instrument-dependent parameters. As a consequence, the following relation holds:

$$\frac{\mathrm{d}I}{\mathrm{d}\omega} = C \frac{\mathrm{d}^2\sigma}{\mathrm{d}\Omega\, \mathrm{d}\omega} = C \frac{k_1}{k_0} \tilde{S}(Q,\omega) \tag{7}$$

where $C \propto \Phi \Delta\Omega \varepsilon(k_1) N$ and, for a monatomic sample, $\tilde{S}(Q,\omega)$ is simply related to the fluid dynamic properties through equation (4), and the knowledge of the numerical values of the coherent and incoherent neutron cross-sections.

3. Models for the neutron double-differential cross-section of dilute H_2

In order to generalize the previous concepts to the case of molecular systems, the first step consists in taking a molecule as the basic unit for dynamical considerations. Thus we will consider a system composed of N identical molecules, each composed of n nuclei. Equation (1) can thus be generalized to the double-differential cross-section per molecule, as

$$\frac{\mathrm{d}^2\sigma}{\mathrm{d}\Omega\, \mathrm{d}\omega} = \frac{k_1}{k_0} \frac{1}{2\pi} \int \mathrm{d}t\, \mathrm{e}^{-\mathrm{i}\omega t} \frac{1}{N} \sum_{\alpha,\beta=1}^{N} \sum_{i,j=1}^{n} \langle b_{\alpha i}^{*} \mathrm{e}^{-\mathrm{i}\boldsymbol{Q}\cdot\boldsymbol{R}_{\alpha i}(0)} b_{\beta j} \mathrm{e}^{\mathrm{i}\boldsymbol{Q}\cdot\boldsymbol{R}_{\beta j}(t)} \rangle \tag{8}$$

where $\boldsymbol{R}_{\beta j}$ and $b_{\beta j}$ are now the position vector and scattering length, respectively, of the jth nucleus in the βth molecule. However, such a straightforward generalization, involving a statistical and quantum average indicated by $\langle \cdots \rangle$, can be easily evaluated only when the eigenvectors describing the global, i.e. vibro-roto-translational–spin, state of a molecule form a complete set, and this condition is not fulfilled, in general, when quantum effects related to the indistinguishability principle are important, as happens typically at low

temperatures [2, 8–10, 13]. In fact, unless nuclei of the same element present in a molecule can be treated as Boltzmann particles, the symmetry requirements for the total molecular wavefunction generally impose a coupling between the total spin state and the roto-vibrational state of the molecule. For homonuclear diatomic molecules such a coupling, often referred to as 'spin correlation', translates into the impossibility of having states with total molecular spin and rotational quantum numbers of different parity, and into the existence of two distinct species for the molecular states, ortho-states and para-states, which follow different probability distributions. A review of the detailed treatment for homonuclear diatomic molecules and the proper generalization of the molecular neutron double-differential cross-section when spin correlations are important, following the guidelines of the YK model, can be found in [13]. Here, the rather high temperature of the sample that we are interested in (room temperature hydrogen) might allow us to assume negligible spin correlations, and to consider the simpler case of Boltzmann particles [10, 13]. However, the uncorrelated-spin treatment is able to predict the total neutron spectra of hydrogen at high temperature to a good approximation, but cannot be used to investigate the details of the individual rotational transitions contributing to the spectrum, which always require, instead, the full spin-correlated treatment and the consideration of the ortho–para-composition of the diatomic fluid, whatever the temperature. Therefore, we recall in the following the basic relations of the YK correlated-spin case, which can be found under few simplifying assumptions, and address the reader to [13, section 3.1] for further details.

The first basic assumption is that the hydrogen molecules of the system behave as *free vibro-rotors*, which is certainly a more than reasonable hypothesis in the low-density case that we are dealing with. This means that the relative orientations of the molecules (intermolecular rotation coupling) and correlations between vibrational states of different molecules can be neglected. Consequently, the translational centre-of-mass dynamics of the molecules is assumed to be completely independent of the individual roto-vibrational and spin states. In this hypothesis, and expressing the position vector $\boldsymbol{R}_{\beta j}$ as the sum of the position vector $\boldsymbol{R}_{\beta}$ of the centre of mass (CM) of the βth molecule and the position vector $\boldsymbol{r}_{\beta j}$ of nucleus j with respect to the CM, it is possible to show that the double-differential cross-section of a molecular sample can be written as [13, equation (4)]

$$\frac{\mathrm{d}^2\sigma}{\mathrm{d}\Omega\,\mathrm{d}\omega} = \frac{1}{2\pi}\frac{k_1}{k_0}\int \mathrm{d}t\,\mathrm{e}^{-\mathrm{i}\omega t}[F_{\mathrm{s}}(Q,t)v(Q,t) + F_{\mathrm{d}}(Q,t)u(Q)] \tag{9}$$

where both $u(Q)$ and $v(Q,t)$ are single-molecule functions, which globally represent the 'molecular cross-sections', and depend on the intramolecular roto-vibrational–spin dynamic features. We note that the free-rotor assumption and the separation into self-molecule and distinct-molecule contributions enable the introduction, as for monatomic systems, of the self-ISF and distinct ISF, $F_{\mathrm{s}}(Q,t)$ and $F_{\mathrm{d}}(Q,t)$, which describe, in this case, the CM translational dynamics of the molecules. Thus, in the molecular case with free rotations, $\tilde{S}(Q,\omega)$ is simply given by

$$\tilde{S}(Q,\omega) = \frac{1}{2\pi}\int \mathrm{d}t\,\mathrm{e}^{-\mathrm{i}\omega t}[F_{\mathrm{s}}(Q,t)v(Q,t) + F_{\mathrm{d}}(Q,t)u(Q)] \tag{10}$$

which, when compared with equation (3), shows a structure fully analogous to that in the monatomic case, except that the coherent cross-section for the distinct term is now a function of Q, $u(Q)$, and the total scattering cross-section (coh + incoh) weighting the self-part is replaced by a function of both Q and time, $v(Q,t)$.

Explicit expressions for the molecular cross-sections, $u(Q)$ and $v(Q,t)$, of H_2 can be obtained by assuming negligible intramolecular vibration–rotation coupling and harmonic vibrations. The diatomic gas is thus treated as a gas of freely rotating harmonic oscillators.

The corresponding quantum-mechanical calculations can be carried out by using the single-molecule roto-vibrational–spin product states (expressed in terms of the rotational, vibrational and molecular spin quantum numbers) $|w\rangle = |JM\rangle|TM_T\rangle|\upsilon\rangle$, of energy E_w given by the sum of the rotational and vibrational energies, $E_w = [E_J + E_{\rm vib}] = [BJ(J+1) - DJ^2(J+1)^2 + \hbar\omega_\upsilon(\upsilon + \frac{1}{2})]$, with ω_υ the frequency of the harmonic oscillator, B the rotational constant and D the centrifugal distortion constant. As anticipated, due to the symmetry restrictions on the molecular wavefunction of hydrogen, the product states $|w\rangle$ do not form a complete set, and only those states where T and J appear with the same parity are admitted.

The quantum calculations finally yield for $v(Q,t)$ [8–10, 12, 13]

$$v(Q,t) = \sum_{J_0 J_1 \upsilon_0 \upsilon_1} {\rm e}^{{\rm i}\omega_{J_0 J_1} t} {\rm e}^{{\rm i}(\upsilon_1 - \upsilon_0)\omega_\upsilon t} f(Q, J_0, J_1, \upsilon_0, \upsilon_1) \tag{11}$$

where subscripts 0, 1 denote quantum numbers before and after the scattering event, respectively, and $\omega_{J_0 J_1} = (E_{J_1} - E_{J_0})/\hbar$ is the rotational transition frequency. We note that excited vibrational states are unpopulated in hydrogen at room temperature; thus all molecules lie initially in the vibrational ground state ($\upsilon_0 = 0$). As a consequence, the function f in equation (11) no longer depends on υ_0, and explicitly reads

$$f(Q, J_0, J_1, \upsilon_1) = s_{(J_0 J_1)} x_{(J_0)} p_{J_0}^{(J_0)} \frac{\alpha^{2\upsilon_1}}{4\upsilon_1!}(2J_1 + 1) \sum_{l=|J_0 - J_1|}^{J_0 + J_1} C^2(J_1 J_0 l; 000)|A_{l,\upsilon_1}|^2 \tag{12}$$

where $\alpha = Q\sqrt{\hbar/(2M\omega_\upsilon)}$, M is the molecular mass, C is a Clebsch–Gordan coefficient, $A_{l,\upsilon_1} = \int_{-1}^{1} {\rm d}\eta\, \eta^{\upsilon_1} {\rm e}^{-\alpha^2\eta^2/2} {\rm e}^{{\rm i}\beta\eta} P_l(\eta)$, with P_l the Legendre polynomial of order l, $\beta = QR_{\rm eq}/2$ and $R_{\rm eq}$ is the equilibrium internuclear distance of the hydrogen molecule in the ground rotational state. Use of a J-dependent equilibrium distance, aimed at accounting for the effects of centrifugal distortion on the internuclear separation, and roughly representable by $R_{\rm eq}^{\rm eff} = \hbar/\sqrt{M[B - DJ(J+1)]/2}$, can be verified to give negligible differences from the calculations using the constant ground-state value $R_{\rm eq}$ for all J. In equation (12), the subscripts and superscripts in brackets mean that the quantities s, x and p_{J_0} vary with the parity of J_0, or with the parity combination of J_0 and J_1 (even–even, odd–odd, even–odd, odd–even). In particular, the coefficients s contain the coherent and incoherent nuclear scattering lengths of the hydrogen nucleus, and have different expressions depending on the above-mentioned parity combinations. The explicit formulae can be found in [13, table 2], using $I = 1/2$ for the nuclear spin. Similarly, the species concentrations x are determined by the parity of the rotational levels [13, table 1], and at room temperature tend to the so-called 'normal' values, which for hydrogen are $x_{\rm even} = x_{\rm para} \to 1/4$ and $x_{\rm odd} = x_{\rm ortho} \to 3/4$. Finally, even and odd rotational initial state probabilities, $p_{J_0}^{\rm even/odd}$, are found to contribute to equation (12), and, along with the species concentrations, determine the different probabilities pertaining to the ortho-molecular and para-molecular states. For instance, $p_{J_0}^{\rm even}$ is given by

$$p_{J_0}^{\rm even} = \frac{(2J_0 + 1)\exp(-\beta E_{J_0})}{\sum_{J_0 \rm even}(2J_0 + 1)\exp(-\beta E_{J_0})},$$

where the denominator can be identified with the even rotational partition function, $Z_{\rm even}$.

As regards $u(Q)$, calculations give, fortunately, a far simpler result [8–10, 12, 13]:

$$u(Q) = b_{\rm coh}^2 A_{0,0}^2. \tag{13}$$

Since $u(Q)$ is time independent, the distinct part in equation (10) reduces to $\tilde{S}_{\rm d}(Q,\omega) = u(Q)S_{\rm d}(Q,\omega)$, which probes the centre-of-mass dynamics of the fluid arising from correlations, ruled by the intermolecular interaction potential, between different molecules. Purely coherent scattering characterizes $u(Q)$ and, consequently, the distinct contribution to the

total double-differential cross-section. As regards the single-molecule term in equation (10), it is seen that the time dependence of $v(Q,t)$ prevents one from deriving an explicit expression in terms of the CM self-dynamic structure factor $S_s(Q,\omega) = \frac{1}{2\pi}\int \mathrm{d}t\, \mathrm{e}^{-\mathrm{i}\omega t} F_s(Q,t)$. However, time enters the expression for $v(Q,t)$ in equation (11) only in complex exponential form; thus it is possible to rewrite the self-part of equation (10) as

$$\begin{aligned}\tilde{S}_s(Q,\omega) &= \sum_{J_0 J_1 \upsilon_1} f(Q, J_0, J_1, \upsilon_1)\frac{1}{2\pi}\int \mathrm{d}t\, \mathrm{e}^{-\mathrm{i}(\omega-\omega_{J_0J_1}-\upsilon_1\omega_\upsilon)t} F_s(Q,t) \\ &= \sum_{J_0 J_1 \upsilon_1} f(Q, J_0, J_1, \upsilon_1) S_s(Q, \omega - \omega_{J_0J_1} - \upsilon_1\omega_\upsilon) \qquad (14)\end{aligned}$$

which corresponds to a sum, over the possible transitions, of single-molecule contributions in which the CM self-dynamic structure factor can effectively be factored out, but explicitly depends, through a frequency shift, on the specific intramolecular transition.

Summarizing the information gathered so far by means of equations (10)–(14), the double-differential cross-section of hydrogen can, according to the YK treatment, be modelled as

$$\frac{\mathrm{d}^2\sigma}{\mathrm{d}\Omega\,\mathrm{d}\omega} = \frac{k_1}{k_0}\left[b_{\mathrm{coh}}^2 A_{0,0}^2 S_\mathrm{d}(Q,\omega) + \sum_{J_0 J_1 \upsilon_1} f(Q, J_0, J_1, \upsilon_1) S_s(Q, \omega - \omega_{J_0J_1} - \upsilon_1\omega_\upsilon)\right] \qquad (15)$$

with f given by equation (12). At extremely low densities, such as those investigated here ($n \sim 0.15$ nm^{-3}), the distinct CM dynamic structure factor tends to vanish. Moreover, the coherent scattering length of the hydrogen nucleus is negligible compared with the incoherent one. The latter does not contribute to the distinct part, while it is contained in the f function weighting the self-terms. Therefore, for dilute H_2, the dynamic response to neutrons is represented by a further simplified model, that is

$$\frac{\mathrm{d}^2\sigma}{\mathrm{d}\Omega\,\mathrm{d}\omega} = \frac{k_1}{k_0}\tilde{S}_s(Q,\omega) = \frac{k_1}{k_0}\sum_{J_0 J_1 \upsilon_1} f(Q, J_0, J_1, \upsilon_1) S_s(Q, \omega - \omega_{J_0J_1} - \upsilon_1\omega_\upsilon), \qquad (16)$$

which retains only the self-contributions to the dynamic structure, as expected for a nearly ideal gas. Accordingly, a suitable representation of the centre-of-mass single-molecule dynamics S_s is, in such conditions, the i.g. model of equation (6), with M replaced by the molecular mass of H_2. With these premises, equations (12), (14) and (16) can be quite straightforwardly computed. The specific parameters and conditions for practical implementation in the present case will be discussed in the following subsection.

No substantial alternatives to the rather detailed quantum method of YK are currently available for predicting the hydrogen spectrum, unless stronger approximations are accepted like the neglect of spin correlations [13, 14] and, further, of the detailed quantum structure of rotational and vibrational levels [4–7]. Under such approximations, simpler expressions for the double-differential cross-section can be obtained, such as the one derived by Krieger and Nelkin [7] by exploiting the mass tensor concept previously introduced by Sachs and Teller [4]. Skipping the quantum calculation of matrix elements involved in the average $\langle\cdots\rangle$ of equation (8), and performing classical thermal averaging over the molecular orientations, the KN result is

$$\frac{\mathrm{d}^2\sigma}{\mathrm{d}\Omega\,\mathrm{d}\omega} = \frac{k_1}{k_0}\sum_{i,j} a_{ij}\, j_0(Q|\boldsymbol{r}_i - \boldsymbol{r}_j|)\mathrm{e}^{-\gamma_{ij}Q^2} S_s^{\mathrm{i.g.}(i)}(Q,\omega), \qquad (17)$$

where i and j run, as before, over the nuclei in the molecule, $\boldsymbol{r}_i$ is the position vector of nucleus i with respect to the CM, $\exp(-\gamma_{ij}Q^2)$ is a Debye–Waller factor resulting from the orientational average of the vibrational wavefunction, j_0 is the zeroth-order spherical Bessel function, $a_{ij} = b_{\mathrm{coh},i}b_{\mathrm{coh},j} + \delta_{ij}b_{\mathrm{inc},i}^2$ and the self-dynamic structure factor is the ideal gas one

of equation (6) with M replaced by $M_i^{(0)} = 3/\operatorname{Tr}\mathbf{M}_i^{-1}$, the latter being the inverse mass tensor for the ith nucleus. According to Sachs and Teller, for hydrogen $\operatorname{Tr}\mathbf{M}_i^{-1} = (1+1+1/2)/m_{\mathrm{H}}$, we thus have $M_i^{(0)} = 1.2m_{\mathrm{H}}$, where m_{H} is the mass of the proton. Equation (17) can indeed be easily calculated; however, it is expected to give a reasonable description of neutron spectra when the incident neutron energy is large compared to the spacing of the rotational states, and when many of these levels are thermally excited.

3.1. Numerical calculation of $\tilde{S}(Q,\omega)$ for H_2 at low density

The fundamental parameters ruling the development of the YK calculations are the temperature T of the fluid and the incident neutron energy E_0. The former determines the initial roto-vibrational state of the sample; the latter defines the possible intramolecular transitions. As mentioned, at room temperature, excited vibrational levels of H_2 are unpopulated; thus the initial value υ_0 of the vibrational quantum number is zero, and the occupation probability of the ground vibrational state is unity for all the molecules in the gas. As a second step, the energy of transition towards excited vibrational states has to be compared with the incident neutron energy E_0, in order to establish whether vibrational transitions can or cannot be induced by the scattering process. Neutrons are unable to excite molecular vibrations in hydrogen if neutron energies below $\hbar\omega_\upsilon = 515.9$ meV [31] are used, as in the case of the present experiment, where incident energies below 60 meV were employed. Therefore, calculations were performed by also taking $\upsilon_1 = 0$ in all the above formulae.

Similar comparisons must be carried out for rotations. In particular, once the even and odd rotational partition functions have been calculated at the given temperature, the initial ortho–para-probabilities $x_{\mathrm{even/odd}}\, p_{J_0}^{\mathrm{even/odd}}$ (see equation (12)) must be analysed in order to decide how many rotational states are thermally populated at a significant level. In the present paper, calculations were typically performed for $J_0 = 0, 1, \ldots, J_{0\,\max}$, with $J_{0\,\max}$ such that $x_{\mathrm{even/odd}}\, p_{J_{0\,\max}}^{\mathrm{even/odd}} \sim 10^{-6}$. Calculation of the above probability shows that, for hydrogen at room temperature, eight rotational levels ($J_0 = 0, \ldots, 7$) are significantly populated.

For each J_0 taken into consideration, one has then to determine the possible final states, J_1. If the neutron energy is so low that no transition towards higher rotational levels is allowed, then J_1 will vary between 0 and J_0 (i.e. only anti-Stokes transitions can occur); otherwise, the incident energy value (which is variable in inverse geometry experiments) is used to establish the maximum J_1 that can be reached, starting from a given J_0. For each E_0 of the experiment, all those final levels satisfying the condition $E_{J_0J_1} = E_{J_1} - E_{J_0} \leqslant E_0 + \Delta$ must be considered, and J_1 will vary, for each J_0, between 0 and $J_{1\,\max}(J_0)$ (i.e. Stokes and anti-Stokes transitions take place). Above, Δ represents a suitable energy able to account for the non-zero width of rotational lines. For instance, one can take $\Delta \approx 3\hbar Q_{\mathrm{el\,max}}(k_{\mathrm{B}}T/M)^{1/2}$, with $\hbar Q_{\mathrm{el\,max}} = 2\hbar k_0 = 2(2mE_0)^{1/2}$, i.e. three times an approximate estimate of the maximum width of the ideal gas spectrum.

When computing inelastic spectra, one has of course to calculate the double-differential cross-section for each (Q,ω) couple probed by the experiment. Consequently, since the energy transfer is defined by $E = \hbar\omega = E_0 - E_1$, with E_1 the final neutron energy, and since Q depends on both ω and the scattering angle θ, through $Q = k_0[2 - \omega/\omega_0 - 2(1-\omega/\omega_0)^{1/2}\cos\theta]^{1/2}$, the above evaluations for the admitted rotational transitions and the consequent calculation of equations (12) and (16) must be repeated for each triplet (E_0, E_1, θ) contributing to the measured spectrum.

Details concerning the numerical calculation of the Clebsch–Gordan coefficients, the integrals $A_{l,\upsilon 1}$, the Legendre polynomials etc can be found in [13]. The hydrogen parameters used in the present computations are given in table 1. As an example, figures 1 and 2 show a

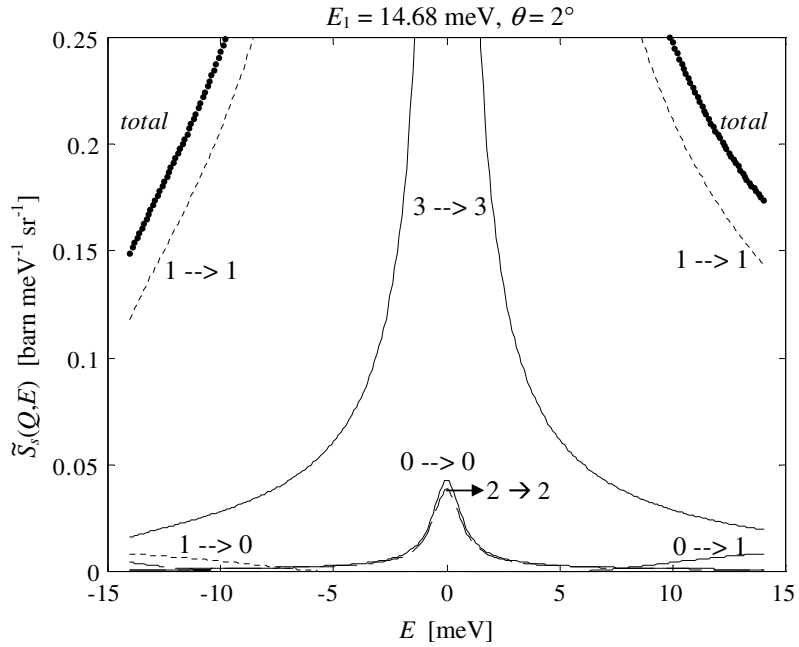

Figure 1. Contribution of the main rotational lines to the total neutron spectrum of hydrogen at room temperature, for fixed final energy neutrons of 14.68 meV and fixed scattering angle $\theta = 2°$. The transition from the initial to the final state, $J_0 \rightarrow J_1$, is indicated for each line. A negligible contribution comes from elastic scattering involving even levels, due to the small coherent cross-section weighting such terms.

Table 1. Rotational constants, equilibrium distance and fundamental oscillator energy of the hydrogen molecule [31] used in the present calculations.

	H_2
B (meV)	7.355
D (meV)	0.005 7
R_{eq} (Å)	0.741 44
$\hbar\omega_\upsilon$ (meV)	515.92

zoom of the total $\tilde{S}_s$ for room temperature H_2 at two different final neutron energies, along with the individual contributions of the rotational lines due to the most relevant $J_0 \rightarrow J_1$ transitions. The line contribution to the total $\tilde{S}_s$ spectrum depends on the initial ortho-probabilities (J_0 odd) or para-probabilities (J_0 even) and, mainly, on the very different cross-section terms (see [13], table 2) pertaining to the various transitions. In particular, all transitions involving at least one odd level depend on the huge incoherent cross-section of the hydrogen nucleus, while those between even states are weighted only by the small coherent cross-section. This explains why in figures 1 and 2 elastic neutron scattering leaving the molecule in an odd state dominates over elastic events involving a molecule in an even rotational level.

4. Experimental details

The experimental spectra from gaseous hydrogen have been collected with the three-axis neutron spectrometer IN3 at the High-Flux Reactor of the Institut Laue-Langevin in Grenoble.

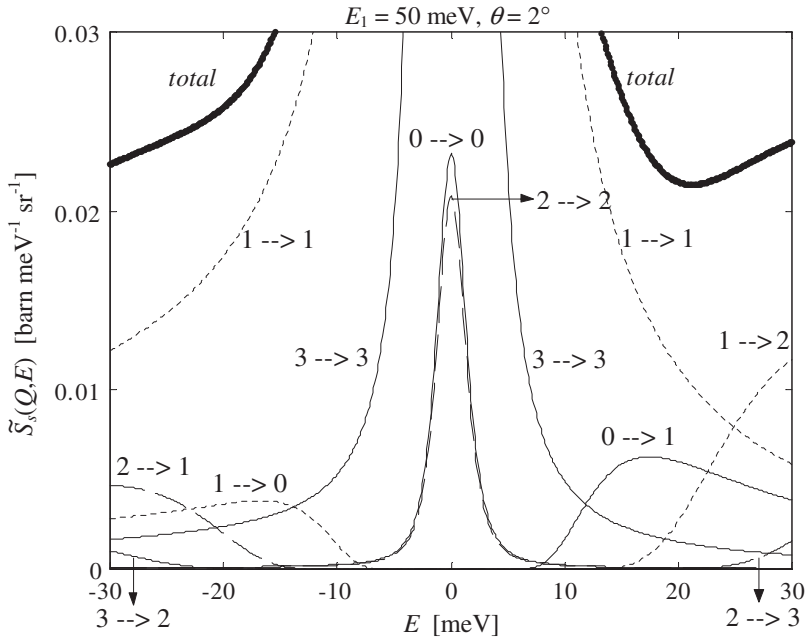

Figure 2. As figure 1, but for fixed final energy neutrons of 50 meV.

The experiment was performed by employing the Cu(111) monochromator, and two different analyser set-ups, namely Cu(111) and PG(002), for fixed final energy scans at $E_1 = 50$ and 14.68 meV, respectively. In the second set-up, a neutron filter could be used in the scattered beam to suppress the higher-order harmonics from the analyser. Quite relaxed collimations, $(40', 40', 60')$ from the monochromator to the detector, could be employed in both cases, due to the broad features of the hydrogen spectrum which do not require extreme instrumental performances in terms of energy resolution. All energy scans were carried out in a constant-θ configuration, which, as will be clear in the following, is particularly suited to the purpose of testing the normalization method discussed in the introduction. At both final energies investigated, spectra were recorded, in particular, for two scattering angles, namely $\theta = 2°$ and 7°. A schematic drawing of the instrument set-up and operation mode adopted is shown in figure 3.

The use of the inverse geometry configuration, i.e. where variation of the energy transfer E is obtained by changing the incident energy E_0 at fixed final energy E_1, requires one to scan the Bragg angle at the monochromator, θ_M, while the Bragg angle at the analyser, θ_A, is kept constant. In the set-up adopted the scattering angle θ was also fixed, at either 2° or 7°; thus the geometrical configuration of the instrument downstream from the monochromator, surrounded by a rectangle in figure 3, was the same for each energy transfer value investigated in the runs, and was simply rotated, as a whole, around the vertical axis at the monochromator, in order to allow the different reflections selected by changing θ_M to be followed.

The constant-θ mode can be an advantage when one wants to avoid even minimum variations of the collected intensities merely due to geometrical effects from one energy point to another in the same scan. Indeed, the way in which the analyser–detector arm 'sees' the sample, during the energy scan, is always the same if θ is constant, independently of the sample shape. A direct consequence of the invariance of the geometrical configuration

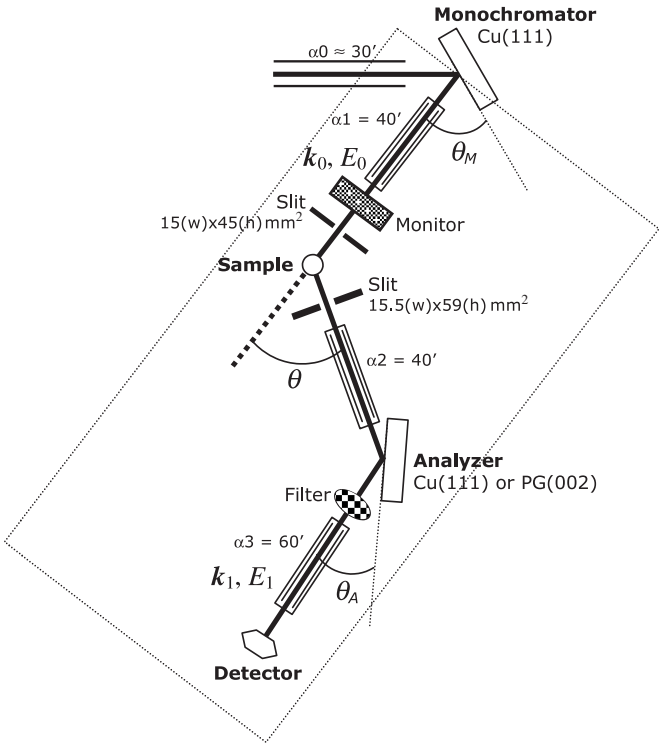

Figure 3. Three-axis spectrometer configuration employed for the neutron measurements on H_2. The Bragg angles at the monochromator and analyser are indicated, as well as the scattering angle θ and the dimensions of the rectangular diaphragms, before and after the sample, for the definition of the incident and scattered beam. Collimation angles are also shown for each arm of the spectrometer. The inverse geometry operation adopted at constant θ implies that changes in the energy transfer E are obtained by changing θ_M, while both θ and θ_A remain unchanged throughout the whole energy scan. A decrease of θ_M gives access to higher energy transfers. In the constant-θ mode, the whole part of the spectrometer surrounded by the dotted rectangle is rotated, rigidly, around the vertical axis, normal to the plane of the figure, at the centre of the monochromator.

coupling the position and orientation of the analyser with the shape and size of the sample is that solid angle effects do not, in principle, affect the measured spectra. Thus, within an energy scan, the (effective) solid angle term $\Delta\Omega$, introduced at the end of section 2, does not contribute, ultimately, to variations of the normalization factor C in the general equation (7). Similarly, the detector efficiency, which depends on the energy of the scattered neutrons, gives a constant contribution to C when the inverse geometry operation of the spectrometer is used, and, more important, the efficiency of the analyser crystal is also kept constant. Conversely, due to the energy dependence of both the flux from the neutron guide and the monochromator crystal reflectivity, the flux Φ at the sample is a function of E_0. This fact, together with the $1/k_0$ variation in equation (7), apparently prevents one from deriving the accurate energy dependence of the absolute scattering efficiency of the sample, i.e. the true scattering law $\tilde{S}(Q, \omega)$, determined by the system response to a constant flux of neutrons. However, the use of a neutron monitor in the incident beam (see figure 3) allows one to adjust the counting time per energy point of a spectrum in such a way as to compensate the intensity variations with E_0. In fact, the monitor counts M_c recorded, for a given E_0, in a time τ, are proportional to $\Phi_0 \tau \eta_{mon}$, with the incident flux at the monitor, Φ_0, approximately equal to that at the sample,

Φ, since the monitor neutron absorption efficiency, η_{mon}, is typically low. Thus, the counts collected, per unit frequency interval, in a time τ, can be written as (see equation (7))

$$I \propto \Phi\tau N\varepsilon(k_1)\Delta\Omega\frac{k_1}{k_0}\tilde{S}(Q,\omega) \cong \frac{M_{\mathrm{c}}}{\eta_{\mathrm{mon}}}N\varepsilon(k_1)\Delta\Omega\frac{k_1}{k_0}\tilde{S}(Q,\omega). \tag{18}$$

Moreover, by taking into account the typical $1/k_0$ dependence of the monitor efficiency, the above intensity reduces further to

$$I \propto M_{\mathrm{c}}N\varepsilon(k_1)\Delta\Omega k_1\tilde{S}(Q,\omega) = \mathrm{const}\cdot\tilde{S}(Q,\omega) \tag{19}$$

which shows how constant-monitor measurements of each energy point in the spectrum provide, in inverse geometry, an intensity that no longer depends on the incident energy and is, to a good approximation, directly proportional to the scattering law. This will make the comparison with the model calculations described in section 3 straightforward, since experimental quantities and calculations are expected to differ, besides energy resolution broadening and other effects accounted for in the following, only by a constant factor over the whole energy range investigated.

The hydrogen sample was maintained at a pressure of 5.88 ± 0.04 bar at $T = 296.5\pm0.5$ K, in a cylindrical container of inner radius $r_{\mathrm{s}} = 8$ mm, sidewall thickness 1 mm and height $h_{\mathrm{s}} = 43$ mm. The thermodynamic conditions of the sample correspond to a molecular number density $n = 0.1431 \pm 0.0005$ nm^{-3}, as obtained from equation-of-state data [32]. Such a value differs from the ideal gas result by less than 0.35%. The material employed for the sample container was an aluminium alloy (Al7075) whose composition was used to evaluate the overall neutron cross-sections, namely, $\sigma_{\mathrm{coh}} = 1.69$ b, $\sigma_{\mathrm{inc}} = 0.02$ b and $\sigma_{\mathrm{abs}} = 0.3$ b at 25 meV, and the atomic number density, $n_{\mathrm{cell}} = 59.6$ nm^{-3}, of the alloy. The sample volume illuminated by the neutron beam (8485 mm^3) was determined by the cadmium masks over the cell, and by the rectangular diaphragm, 15 mm $\times$ 45 mm, defining the dimensions of the incident beam.

In both the above-mentioned set-ups, and for each scattering angle, neutron spectra were also collected for the empty container and for a rolled thin sheet (0.15 mm thick) of vanadium placed inside the cell. The raw data from hydrogen, vanadium and the empty container are compared in figures 4 and 5.

The vanadium runs were performed, as usual, in order to check the spectrometer energy resolution in the set-ups adopted. Subtraction of the vanadium spectra for the background, including the scattering from the container, and multiple scattering, along with corrections for absorption and other effects, as outlined in the following section, provided, as expected, a Gaussian-shaped energy distribution of the single-scattering intensity from the vanadium sample. By means of Gaussian fits to the vanadium single-scattering intensity, shown in figure 6 for the two final energies, we thus derived the standard deviation corresponding to the instrument elastic energy resolution in each set-up. The dependence of the width on the scattering angle is negligible, and the fits provide an energy resolution of 2.74 and 0.73 meV (FWHM) at 50 and 14.68 meV, respectively.

5. Data analysis

The use of the general equation (7) or, as in the present case, equation (19), for comparison between experiment and models of $\tilde{S}(Q,\omega)$ requires the determination of the ideal intensity from the sample, free from absorption effects, and due to singly scattered neutrons of well-defined incident energy. Consequently, the raw neutron data must be corrected for background, container scattering, attenuation effects and multiple scattering. Also, instrumental resolution

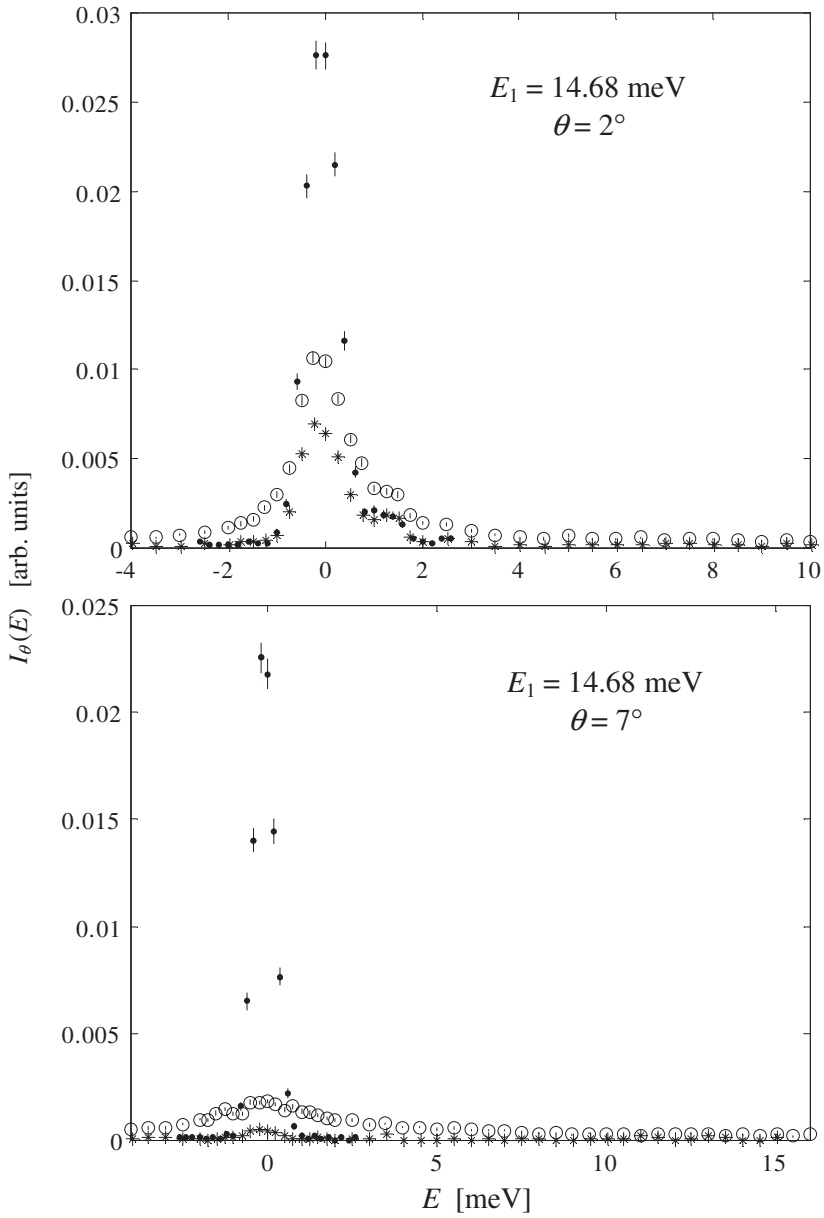

Figure 4. Raw intensities from H_2 (circles) and vanadium (dots) in the container, and the empty cell (stars), at 14.68 meV final energy and scattering angles of 2° (upper frame) and 7° (lower frame).

broadening of the experimental quantities must be considered. Moreover, the possible presence in the incident beam of a non-negligible fraction of neutrons characterized by an energy differing from the nominal one should also be taken into account, at least in an approximate way. In the following subsections we describe the procedures adopted for all the above corrections, starting from the last one.

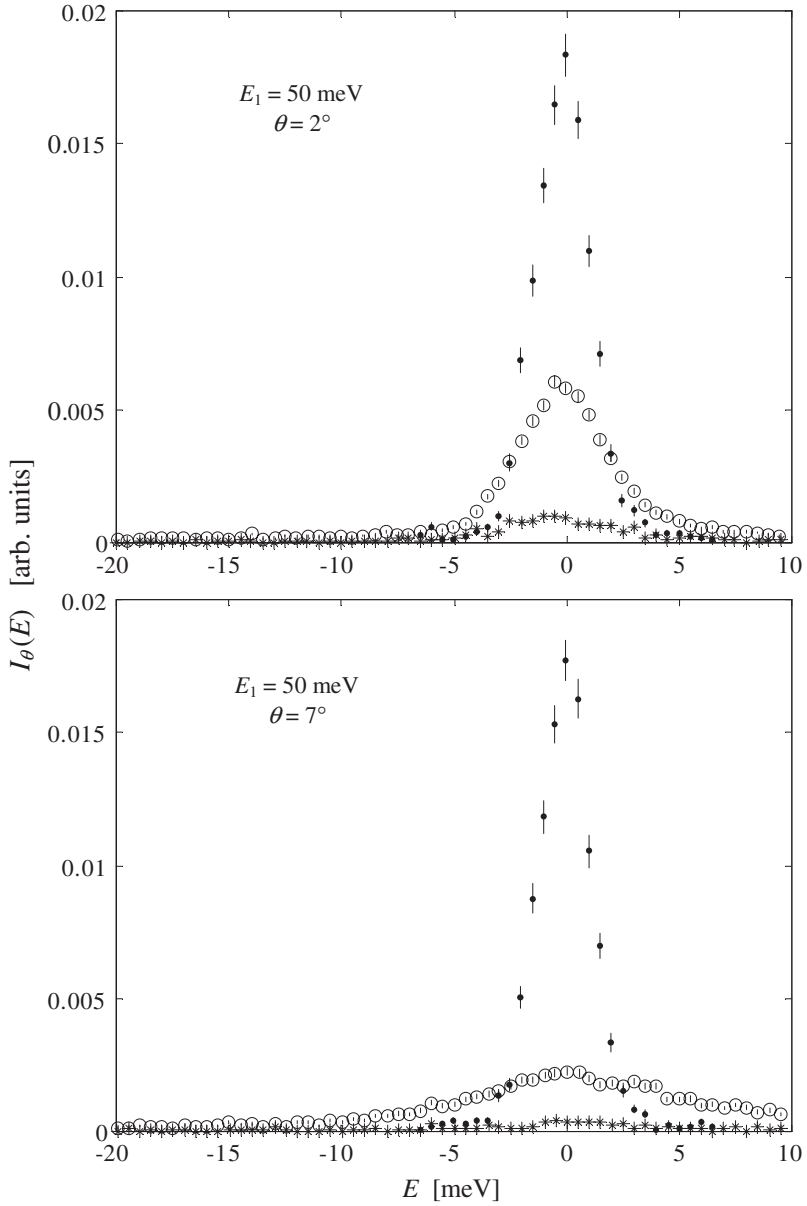

Figure 5. As figure 4, but at 50 meV final energy.

5.1. Correction for incident beam energy contamination

On three-axis spectrometers, selection of the incident neutron energy is performed by means of Bragg reflection at a crystal monochromator. Thus, other-order reflections can give, in certain conditions, a non-negligible contribution to the energy composition of the reflected beam. The IN3 spectrometer of ILL is in the Guide Hall, and typically the flux on a neutron guide at relatively large energies (e.g. >80 meV) is limited. Conversely, the flux of lower-energy neutrons is quite important, with a peak around 35 meV for the guide of IN3. As a

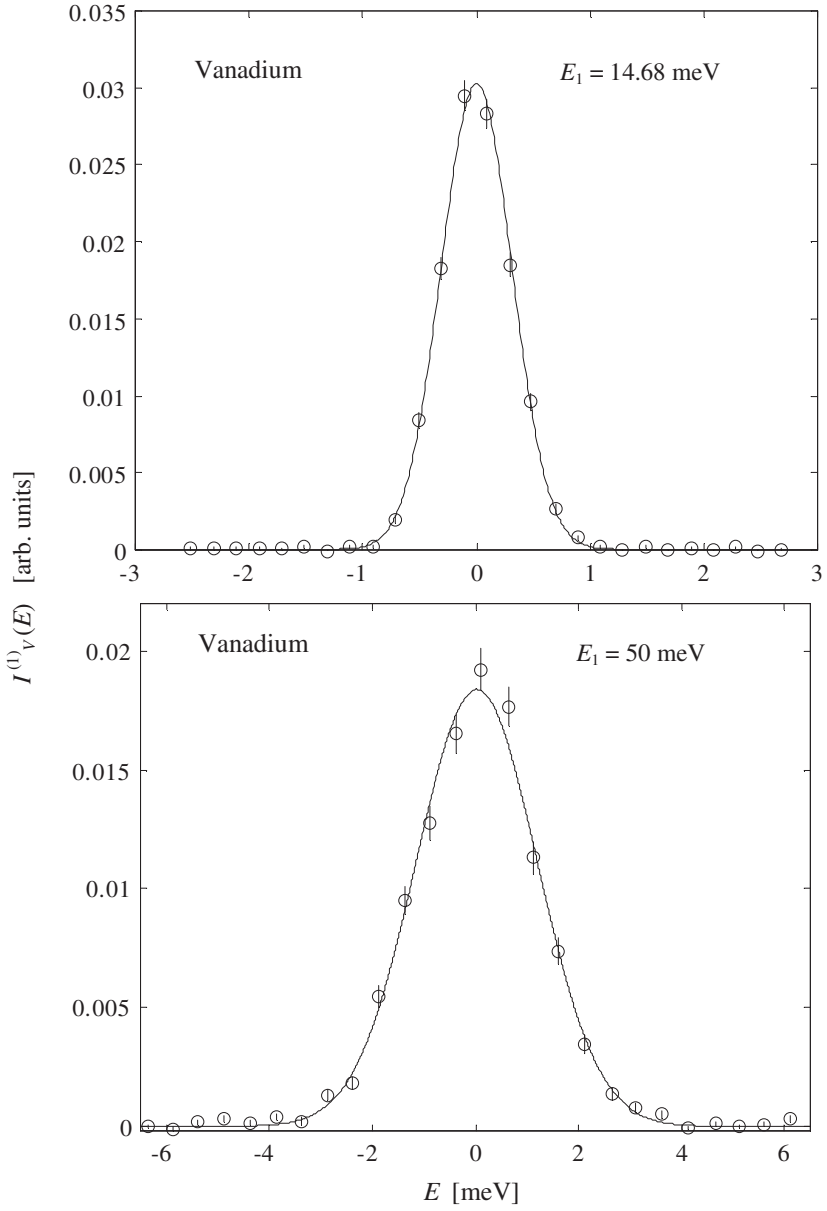

Figure 6. Experimental single-scattering intensity of the vanadium sample (circles with error bars) and Gaussian fit to the data (solid line), at 14.68 meV (upper frame) and 50 meV (lower frame) final energy.

consequence, contamination of the beam by neutrons of energy differing from the working one starts to have a role when the monochromator, along with the wanted reflection, can also select neutrons with energies not too far from the above peak value. In our case, the incident energies required for, for instance, elastic ($E_0 = E_1$) scattering were 14.68 and 50 meV in the two sets of measurements, both employing the (111) reflection of the Cu monochromator. The main contamination could therefore come from the neutrons reflected by the set of planes with

Miller indices (222), i.e. from the $\lambda/2$ neutrons. At 50 meV nominal energy, $\lambda/2$ neutrons correspond to 200 meV energy, which is well above the energy value of the peak in the flux distribution from the guide. Conversely, at 14.68 meV, $\lambda/2$ neutrons correspond to 58.7 meV energy, and can contribute appreciably to the incident beam. Of course, these values give only an indication, since in inverse geometry the nominal incident energy is scanned both below and above the one corresponding to elastic scattering. This should also help with remembering why, in such an operation mode, a neutron filter cannot efficiently be used in the incident beam. The main effect of the presence of higher-order neutrons in the beam is that these are also detected by the incident beam monitor, which is used to determine the counting time for each data point. For a correct normalization of data taken with variable E_0, it is thus necessary to correct the monitor counts in order to derive the value that would be measured in the absence of contamination. Retaining only the contributions of λ and $\lambda/2$ neutrons, the effective monitor counts are given by

$$M_c \propto (\Phi_\lambda \eta_{mon\lambda} + \Phi_{\lambda/2}\eta_{mon\lambda/2})\tau_{\lambda+\lambda/2}.$$

In the absence of $\lambda/2$ contamination, the same monitor counts would be reached in a time τ_λ such that $M_c \propto \Phi_\lambda \eta_{mon\lambda}\tau_\lambda$, i.e. in a longer time. Since the neutron intensity is proportional to the counting time, we can thus write the intensity I^{corr} that would correspond to M_c counts of λ neutrons only as

$$I^{corr} = I^{meas}\frac{\tau_\lambda}{\tau_{\lambda+\lambda/2}} = I^{meas}\frac{\Phi_\lambda + \Phi_{\lambda/2}/2}{\Phi_\lambda} \tag{20}$$

where we used the relation $\eta_{mon\lambda} \propto \lambda$.

To perform the above correction we thus need to know the experimental value of the flux due to λ and $\lambda/2$ neutrons separately, for all the nominal $\lambda(E_0)$ values used in the measurements. An estimate can be obtained by means of specific transmission measurements using the Cu monochromator and a set of identical Pyrex slabs, following the procedure introduced in [33]. Since the transmitted intensity depends on the energy and the number of slabs, higher-order contamination can be quantified provided that the Pyrex attenuation coefficient, $\mu(\lambda) = n\sigma_t(\lambda) \approx n\sigma_s + n\sigma_{abs}(\lambda)$, is known. The latter can be measured directly by means of further transmission runs, with and without one slab, at wavelengths where either a neutron filter after the monochromator can be used (e.g. with a graphite filter at the two 'magic' wavelengths 1.53 and 2.36 Å) or the higher-order contamination is expected to be negligible (i.e. at the lowest wavelengths on a neutron guide). By performing such measurements we were able to estimate the different order contributions to the measured flux, plotted in figure 7 for the two non-negligible components. Since second-order reflections from the Cu(111) monochromator are found to contribute only below 20 meV incident energy, the above-mentioned correction of the neutron intensities will be significant, in our case, mainly for the 14.68 meV measurements. The ratio $\Phi_{\lambda/2}/\Phi_\lambda$, needed for the correction described by equation (20), is plotted as an inset of figure 7, along with a fit of the experimental results by means of the empirical model function $a(2\pi/\lambda)^b$, which provided $a = 626$ and $b = -7.83$, for wavelengths measured in Å.

Figure 8 shows the effect of this correction on the raw H_2 spectra at $\theta = 2°$, for 14.68 and 50 meV. As already observed, the correction is important only for the lower-energy measurements. Comparable effects influence also the empty container and vanadium spectra.

5.2. Evaluation of absorption and multiple-scattering effects

The self-attenuation of the sample–container system, as well as that of the empty container, has been calculated, as a function of the energy transfer, according to the generalization for inelastic

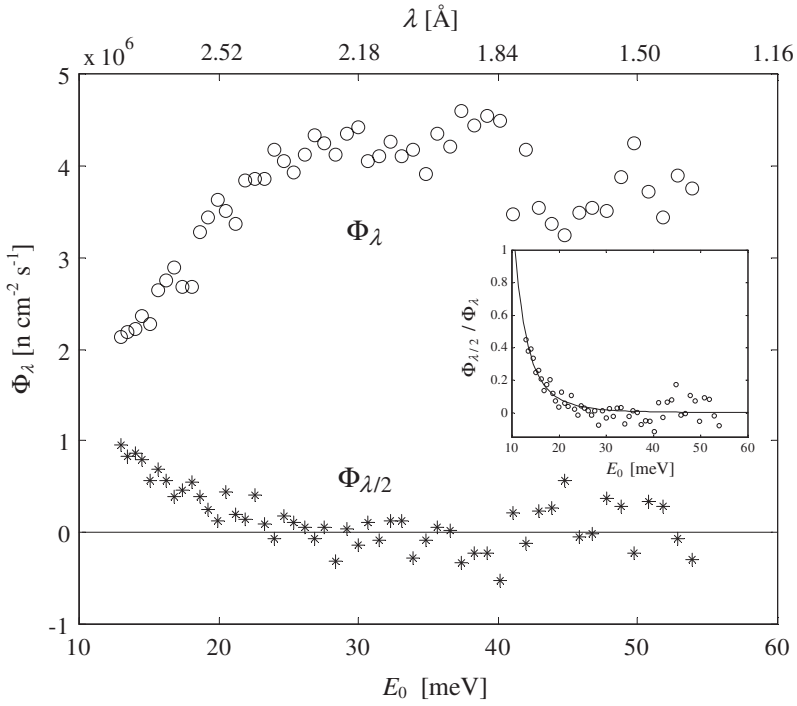

Figure 7. Experimental flux components due to λ (circles) and λ/2 (stars) neutrons from the Cu(111) monochromator, at various nominal wavelengths. It can be observed that second-order reflections have a non-negligible role below (above) 20 meV (2.5 Å). The inset shows experimental results (circles) for the ratio of second-to first-order neutrons contributing to the flux, and the fit of the data (solid line) with the empirical model $a(2\pi/\lambda)^b$.

scattering of the well-known Paalman–Pings coefficients $A_{\alpha,\beta}$ [34, 35], where α and β indicate, respectively, in which element the scattering takes place and where attenuation occurs. For instance, the scattering from the sample alone will be generally attenuated both in the sample itself and in the container. By assuming for the moment only single-scattering events, the sample contribution to the measured intensity can be written as $I^{(1)}_{\mathrm{s,sc}} = A_{\mathrm{s,sc}} I^{(1)}_{\mathrm{s}}$, where sc indicates that both the sample (s) and the container (c) contribute to the signal attenuation, while $I^{(1)}_{\mathrm{s}}$ is the sought-for corrected quantity, i.e. that related to the double-differential cross-section of equation (7). Similar equations can be written for the scattering from the full or empty container. It can be shown that the calculation of the Paalman–Pings coefficients reduces to the evaluation of multidimensional integrals, over the illuminated volume of the specific scattering element (s or c), of the neutron transmission along the incident and scattered paths. For example, a simplified version of $A_{\mathrm{s,sc}}$ is

$$A_{\mathrm{s,sc}} = \frac{1}{V^{\mathrm{ill}}_{\mathrm{s}}} \int_{V^{\mathrm{ill}}_{\mathrm{s}}} \mathrm{d}V^{\mathrm{ill}}_{\mathrm{s}} \exp[-\mu^{\mathrm{c}}(E_0) L^{\mathrm{c}}_{\mathrm{inc}} - \mu^{\mathrm{c}}(E_1) L^{\mathrm{c}}_{\mathrm{scat}}] \exp[-\mu^{\mathrm{s}}(E_0) L^{\mathrm{s}}_{\mathrm{inc}} - \mu^{\mathrm{s}}(E_1) L^{\mathrm{s}}_{\mathrm{scat}}]$$

where we explicitly indicated the energy dependence of the attenuation coefficient μ of the sample and container (superscripts s and c), before and after the scattering event, and we subdivided the distances L travelled in each material into incident and scattered paths, depending on the specific coordinates of the scattering point over the available illuminated volume $V^{\mathrm{ill}}_{\mathrm{s}}$.

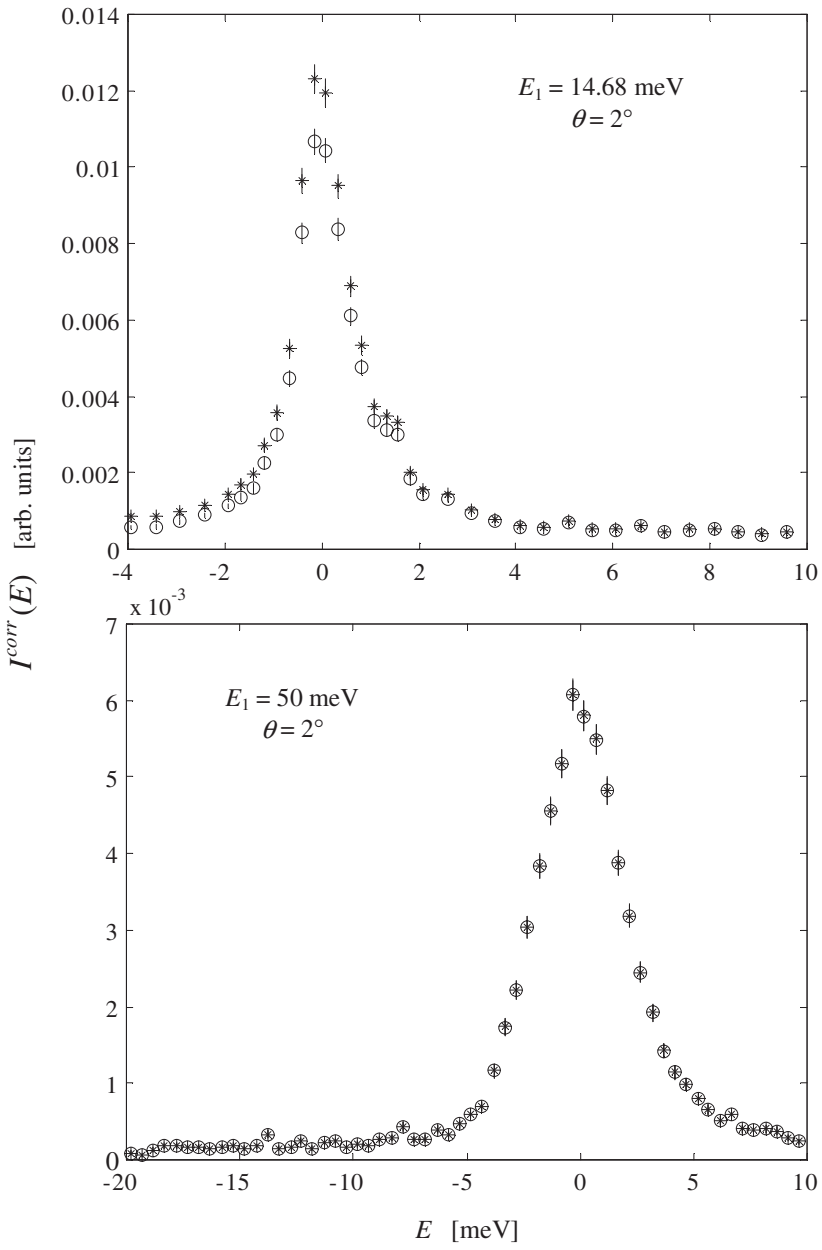

Figure 8. Raw data from H_2 in the cell before (circles) and after (stars) correction for the second-order contribution to the incident monitor counts, according to equation (20). The upper figure shows how the correction visibly modifies the original data at 14.68 meV final energy, while the lower figure confirms that such a correction is unimportant at the higher energies (stars and circles nearly coincide).

Calculations of this kind can be efficiently performed, for any sample and container shape, and for each data point of the experimental spectrum (i.e. for each specific triplet E_0, E_1, θ, defining a point of the energy scan), by means of Monte Carlo integration. The

energy dependence of the Paalman and Pings coefficients, usually rather weak, turned out to be negligible, with typically less than 0.2% variations, for the hydrogen sample. Similar calculations were, of course, performed to evaluate the absorption coefficients in the presence of the vanadium sample.

The evaluation of multiple scattering can be addressed in a conceptually similar way, with the difference that the scattering law must be included in the calculations. We first note, however, that the scattering power of our dilute sample was, as expected, rather low (∼3%). Consequently, the sample multiple-scattering contributions to the measured intensity are comparably weak, while a more important role is played, in our conditions, by multiple-scattering events involving the container. In any case, the rather weak overall effect of multiple scattering in the present experiment allowed us to concentrate on the calculation of the double-scattering intensities only, and to neglect higher-order multiple processes.

In analogy with the previous calculations, the attenuated double scattering from the sample can, for instance, be schematized as (ss means that scattering takes place twice in the sample only)

$$I_{\mathrm{ss,sc}} \propto n^2 \int_{V_{\mathrm{s}}^{\mathrm{ill}}} \mathrm{d}V_{\mathrm{s}}^{\mathrm{ill}} \int_{V_{\mathrm{s}}} \mathrm{d}V_{\mathrm{s}}\, \exp[-\mu^{\mathrm{s}}(E_0)L_{\mathrm{inc}}^{\mathrm{s}} - \mu^{\mathrm{c}}(E_0)L_{\mathrm{inc}}^{\mathrm{c}}] \times \int_0^{+\infty} \mathrm{d}E_{\mathrm{int}}\, \frac{\exp[-\mu^{\mathrm{s}}(E_{\mathrm{int}})L_{\mathrm{int}}]}{L_{\mathrm{int}}^2} \frac{\mathrm{d}^2\sigma}{\mathrm{d}\Omega\,\mathrm{d}E'}\bigg|_{\theta 1} \frac{\mathrm{d}^2\sigma}{\mathrm{d}\Omega\,\mathrm{d}E''}\bigg|_{\theta 2} \times \exp[-\mu^{\mathrm{s}}(E_1)L_{\mathrm{scat}}^{\mathrm{s}} - \mu^{\mathrm{c}}(E_1)L_{\mathrm{scat}}^{\mathrm{c}}]$$

where the second integration over the whole sample volume, V_{s}, takes into account that the second scattering point can be anywhere in the sample, independently of the incident beam dimensions. With respect to the attenuation coefficient case, here there is also an integral over all the possible intermediate energies of the neutron, E_{int}, between the first and second scattering events, as well as the transmission term related to the path L_{int} travelled between the two scattering points. Finally, the intensity depends on the sample dynamic response at both scattering points, where energy transfers are given, respectively, by $E' = E_0 - E_{\mathrm{int}}$ and $E'' = E_{\mathrm{int}} - E_1$. The specific scattering angles of the two events are also indicated.

In the case of dilute hydrogen we are particularly lucky since, unlike in the usual situation in neutron experiments, an extremely realistic model of the sample scattering law for the evaluation of the double-scattering intensity is provided by equations (6) and (16). Similarly, the scattering from the container is also practically known, and can be modelled as predominantly elastic, to a good approximation. With these ingredients, we calculated, by Monte Carlo integration, the double scattering for each possible combination of the elements where first and second scattering can occur (ss, sc, cs, cc). The only slight complication arose from the extremely wide range of E_{int} values needed to perform with good accuracy the intermediate integration over the energy. In fact, E_{int} represents the incident energy for the second scattering event and, since it can be quite high, the corresponding calculations of $\frac{\mathrm{d}^2\sigma}{\mathrm{d}\Omega\,\mathrm{d}E''}$, through equation (16), can involve many rotational transitions. In particular, we estimated that for E_{int} values up to 450 meV, non-negligible contributions to the quoted integral were possible. Thus, our model for the double-differential cross-section was appropriately implemented for such a high incident energy, and required the consideration of initial and final rotational levels such that $J_0 = 0, \ldots, 7$ and $J_1 = 0, \ldots, 10$, while vibrational transitions are still frozen.

We finally give in figure 9 an example of the results, showing the calculated double-scattering components at the nominal angle of 2° and 50 meV final energy. The double scattering from the (full) container, broadened by the instrumental resolution, dominates over other multiple processes in the quasi-elastic range, and for this reason we show in the inset

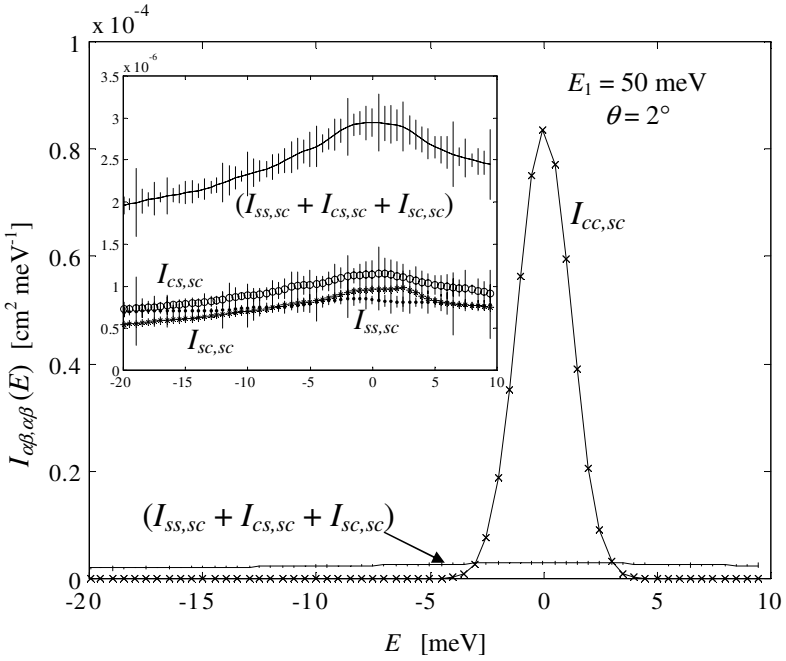

Figure 9. Results of the Monte Carlo calculation of the double-scattering contributions from the sample–container system, at 2° and 50 meV final energy. The double events in the container (line with crosses) $I_{cc,sc}$ are dominant in the quasi-elastic region, while the total double scattering involving the sample ($I_{ss,sc} + I_{cs,sc} + I_{sc,sc}$) is an almost constant background. The inset shows the details for $I_{ss,sc}$ (dots with error bars), $I_{sc,sc}$ (stars with error bars) and $I_{cs,sc}$ (circles with error bars), compared with their sum.

a zoom of the energy dependence of the scattering from the sample and of cross-sample–container contributions.

Given the above calculations, and the corresponding simpler evaluations, in consistent units, of the single-scattering intensity from the sample–container system, a useful quantity is the double-to-single-scattering ratio:

$$\delta_{sc} = \frac{(I_{ss,sc} + I_{sc,sc} + I_{cs,sc} + I_{cc,sc})_B}{(I^{(1)}_{s,sc} + I^{(1)}_{c,sc})_B}$$

where with the subscript B we explicitly indicate that all calculated quantities need to be broadened according to the instrumental resolution, in order to make them comparable with the energy distribution of the measured spectra. Indeed, since calculations cannot take into account the true flux and other experimental factors, i.e. calculated intensities are not in 'experimental units', the ratio gives anyway correct information on the weight that the multiple scattering has in the real measurements (of the order of 2%, globally, in our conditions). This information can thus be used to derive, finally, the sample single-scattering intensity, which can be shown to be related to experimental and calculated quantities by

$$I^{(1)}_s \approx \frac{1}{A_{s,sc}}\left[\frac{I^{corr}_{sc}}{1+\delta_{sc}} - \frac{A_{c,sc}}{A_{c,c}}\left(\frac{I^{corr}_{c}}{1+\delta_c}\right)\right] \tag{21}$$

where I^{corr}_{sc} and I^{corr}_{c} correspond, respectively, to the experimental spectra, corrected for beam contamination (see the previous section), of the sample–container system and of the empty cell, while δ_c is the empty-cell analogue of δ_{sc}. The above equation holds also for the vanadium

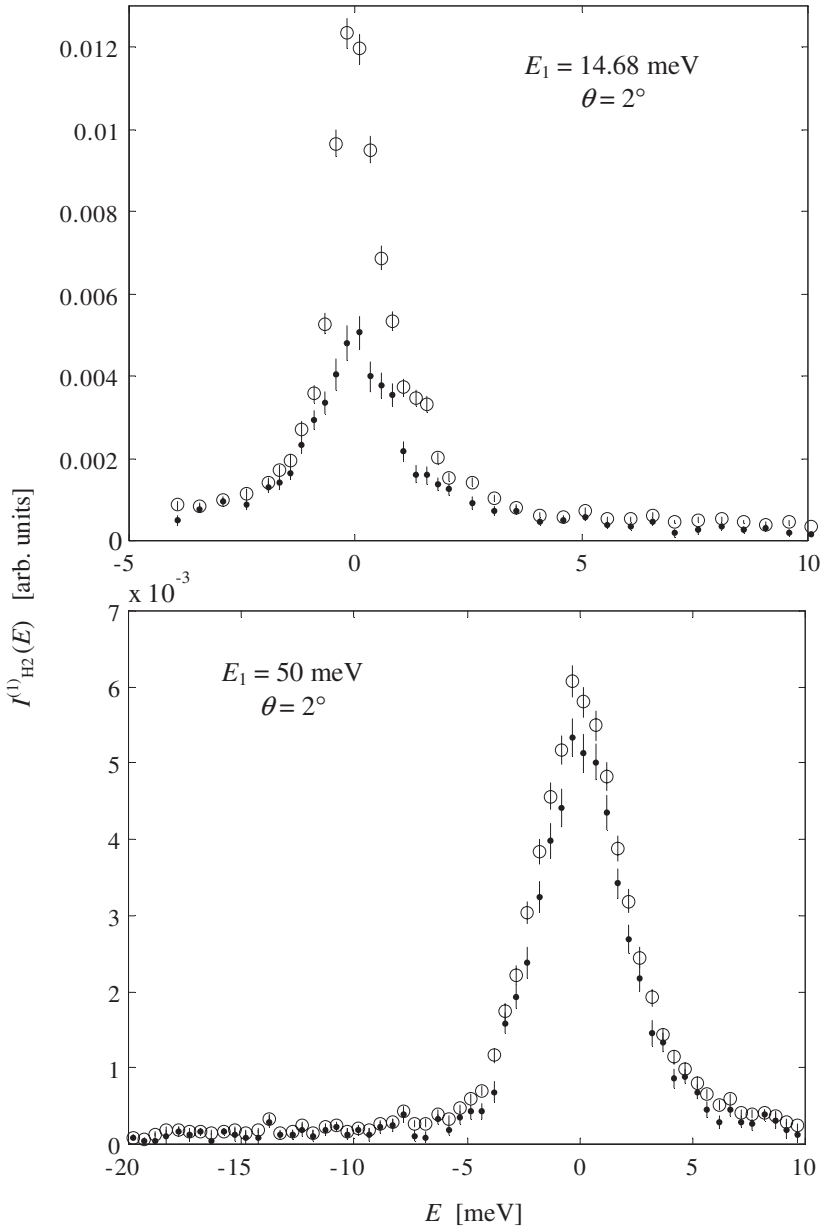

Figure 10. Single-scattering intensity of the hydrogen sample (dots with error bars) according to equation (21), at 2° and the two final energies of the experiment. Circles represent the measured spectra before subtraction of the container and correction for multiple scattering and attenuation effects. The important difference between the raw and corrected data, visible at 14.68 meV (upper frame), is mainly due to the considerable scattering from the container in such conditions.

sample, and was used, together with the corresponding calculations, to derive the spectra already shown in figure 6. To give an idea of the overall effect of the calculated corrections and of container subtraction, we compare, in figure 10, the raw I_{sc}^{corr} and single-scattering $I_s^{(1)}$ data for hydrogen at the two experimental final energies and 2°. In the case of the 14.68 meV

data, we recall that the scattering from the container has an important role at such a scattering angle (see also figure 4, upper frame).

6. Results and conclusions

As explained in the discussion of equation (19), the resolution-free single-scattering intensities are expected to be proportional to $\tilde{S}$ and, in the present case of dilute hydrogen, are proportional in particular to $\tilde{S}_s$, for which we described two models in section 3. It is thus straightforward to investigate the suitability of the methods for the description of the experimental line-shapes, since, once broadened according to the instrumental resolution, the models should reproduce the single-scattering data within a constant factor. With this purpose, we performed fits of the $I_s^{(1)}$ data by means of the simple function $K(\tilde{S}_s^{calc})_B$, with K being the best-fit constant to be determined, and $(\tilde{S}_s^{calc})_B$ the calculated scattering law (equations (16) or (17), and (6)), after energy resolution broadening. The latter has of course a limited effect on the calculations, since the hydrogen model spectra are quite broad by themselves. It is important to observe that the above one-parameter function is far from being 'flexible', in the sense that it is unable to hide even small discrepancies between the shape of the experimental spectra and that of the calculated versions.

The comparison between data and calculations is shown in figures 11 and 12, for the various set-ups of the experiment. In each figure we report also the specific values, K_{YK} and K_{KN}, of the best-fit constant found either using the YK or the KN model. A good agreement with the YK calculations is found in all conditions investigated, even at low final energy and at the lower scattering angle, thus proving that such a model can be reliably employed in small-angle experiments and satisfactorily reproduces the experimental line-shape of dilute H_2. In contrast, the KN result typically provides an underestimation of the peak intensity. Discrimination between the two models in the present kinematic conditions thus becomes clear at the level of the dominant rotational contributions characterizing the quasi-elastic region, where KN is clearly less effective. Conversely, the present results do not show convincing evidence, within the experimental uncertainties, of the expected loss of accuracy of the KN predictions in the energy-gain region, where the incident neutron energy here becomes inferior to or comparable with the transition energies [2, 7]. Nonetheless, the overall spectra are better accounted for by the YK model, as confirmed also by a systematic, though limited, increase of the χ^2 that we found in passing from the YK fits to the KN ones. It is worth recognizing however that, despite the strong approximations of the KN theory and the effects that these have on the details of the energy distribution, the model is anyway able to roughly describe the measurements at the level of the integrated spectra, i.e. of the differential cross-section $d\sigma/d\Omega$.

The present experimental results, combined with the YK treatment, clearly show that low-density H_2 is more than appropriate for normalization purposes. It would be interesting to have another reliable reference sample in order to perform a cross-check with hydrogen. Unfortunately, at the low scattering angles investigated here, vanadium is inappropriate for this purpose, because it is difficult to disentangle hypothetical problems in the normalization procedure with hydrogen from those related to the spurious small-Q scattering from vanadium mentioned in the introduction. Indeed, from our measurements on the rolled vanadium slab and an approximate evaluation of the atoms exposed to the beam, we were able to attempt a normalization of the vanadium data with hydrogen, and derive an experimental estimate of $\sigma_s/4\pi$, for comparison with the tabulated value for vanadium (0.406 b sr^{-1}). The results, plotted in figure 13, confirm the difficulties mentioned above, since a visible difference can be observed at the smallest scattering angle and at low energy, i.e. for the lowest Q value probed

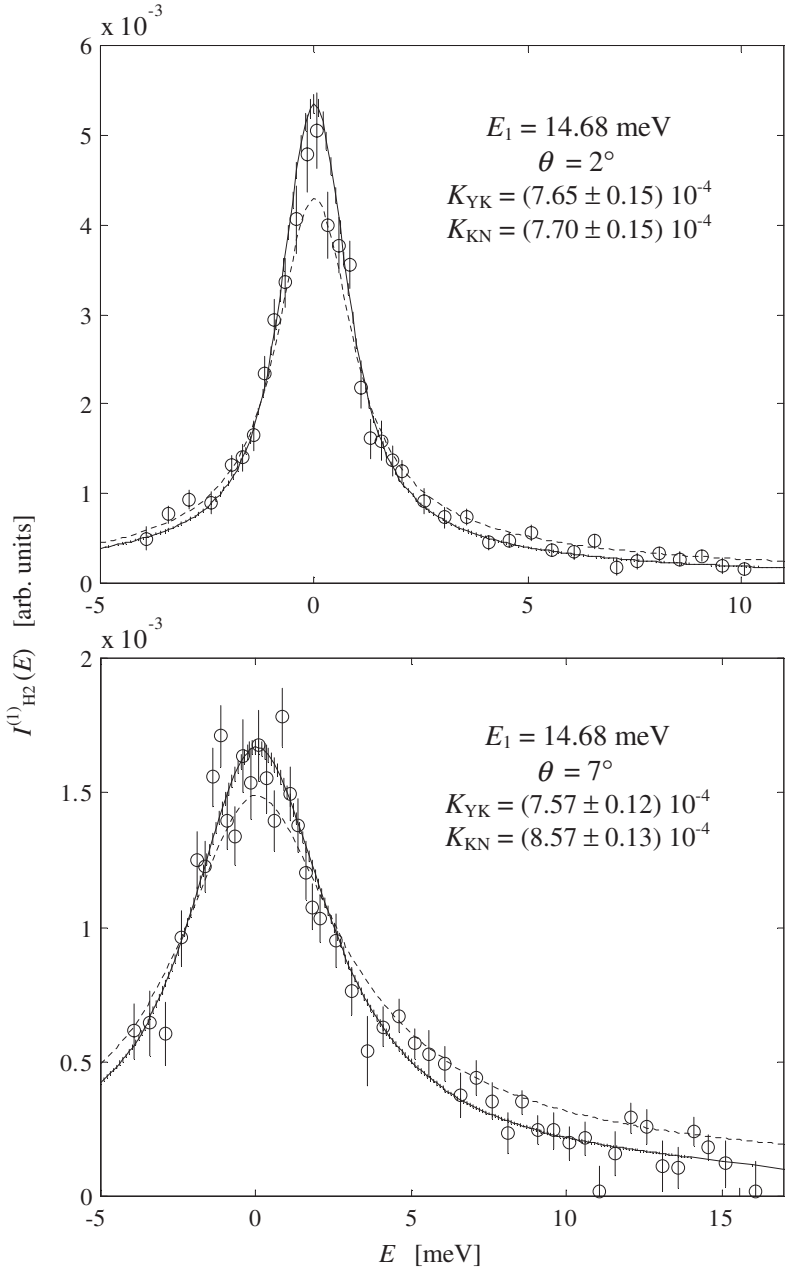

Figure 11. Single-scattering intensity of the hydrogen sample at 14.68 meV (circles with error bars), compared, at both scattering angles, with the YK (solid line with error bars) and KN (dotted line) model calculations, after resolution broadening. The factors of proportionality, K_{YK} and K_{KN}, between data and calculations (see the text) are shown in each frame. The uncertainty in the value of K_{YK} determines the error attributed to the corresponding model line-shape.

by the experiment. This fact appears only as further evidence that experimental intensities from vanadium at small Q typically exceed the expected isotropic value, rather than indicating

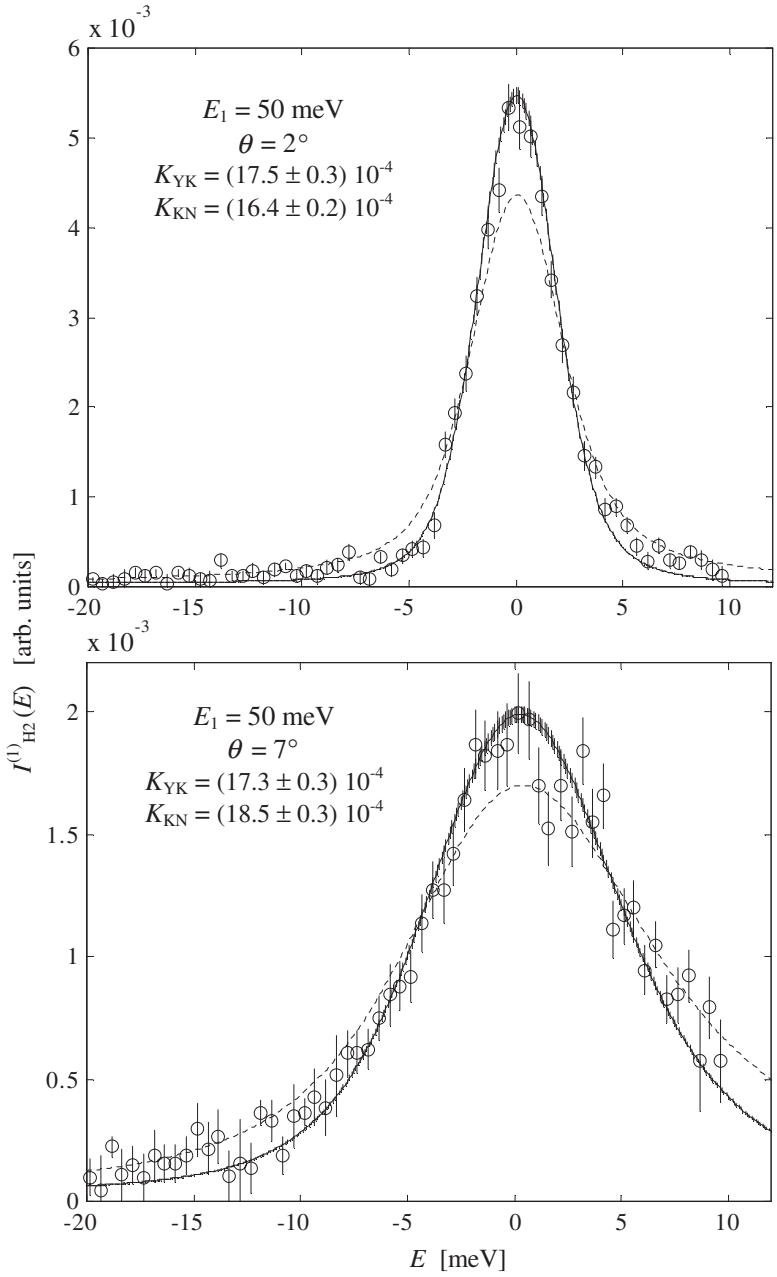

Figure 12. As figure 11, but for 50 meV final energy.

slight inadequacies of the hydrogen YK model. On the contrary, the latter is found to provide, for the H_2 measurements performed at a given final energy, the same fit quality and, more important, the same K_{YK} values at both scattering angles, which is an extremely significant result if one considers that, in our conditions, solid angle variations were absent not only within an energy scan, but also between scans at different θ, thanks to the nearly cylindrical shape

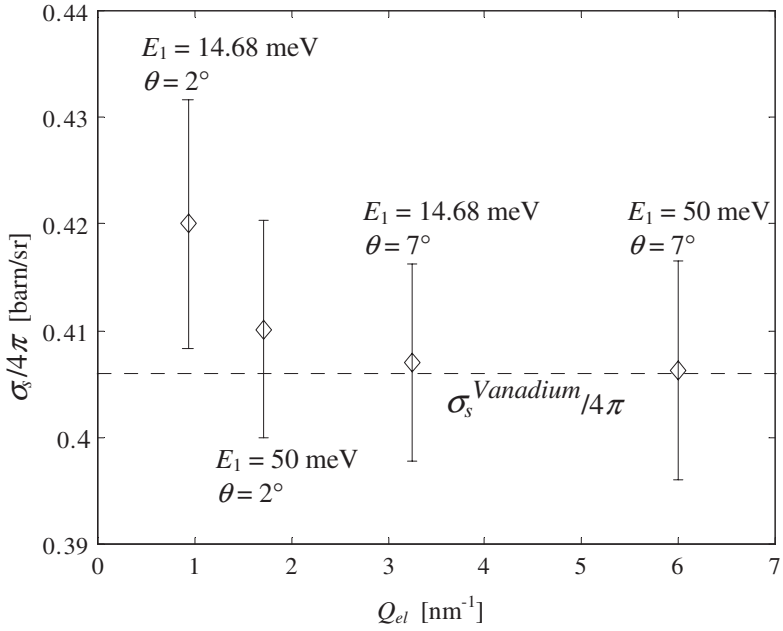

Figure 13. Scattering cross-section of vanadium as derived by hydrogen normalization of the measurements on the rolled slab V sample, as a function of the elastic wavevector transfer values probed by the experiment. The dashed line is the literature value for $\sigma_s/4\pi$ of vanadium.

of our illuminated sample (see section 4 and figure 3). Thus, the YK model ensures a correct line-shape description at all Q values, with fit results strongly supporting a high consistency between experimental findings and theoretical modelling, while the same does not happen with the KN results. The overall accuracy of the hydrogen method can therefore be estimated from the relative error on the proportionality factor K_{YK}, which turns out to range between 1.5 and 2%.

With the present fundamental test of the scattering law of dilute H_2, the power of the hydrogen calibration technique in neutron spectroscopy becomes even more evident when the more complex case of direct geometry spectrometers with two-dimensional detection is considered. The availability of a reference sample characterized by a broad energy spectrum like H_2, and the detailed knowledge of its scattering law for each (E_0, E_1, θ) triplet, allows in fact for an extremely accurate 'point-by-point' normalization of experimental intensities, capable of including even the slightest variations in solid angle and efficiency (consider equation (18), for fixed initial energy neutrons) from one detector cell to the other, over the whole available area. This means, in other words, that individual normalization factors can be assigned to the sample intensities, for each E value and for each detector element, with unprecedented accuracy.

For completeness, we show finally in figure 14 the resolution-free $\tilde{S}_s(E)$ of dilute H_2 in absolute units, calculated over the experimental energy range. An estimation of the uncertainties could be performed by exploiting the experimental information, i.e. by assigning error bars depending on both the experimental error in the $I_s^{(1)}$ data and the uncertainty in the fitted K_{YK} values.

This first determination of the self-dynamic cross-section of molecular hydrogen at room temperature, carried out at the top performances of neutron spectrometry and compared with

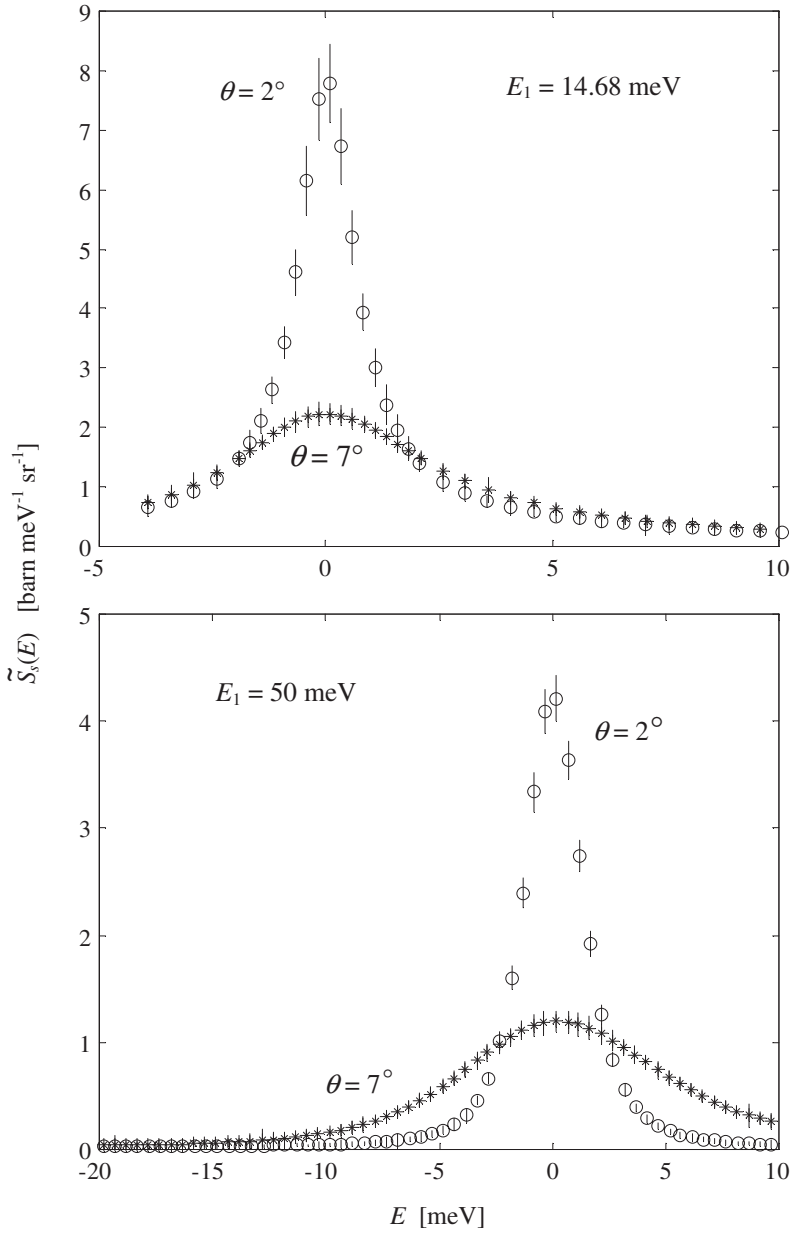

Figure 14. Resolution-free self-dynamic neutron cross-section of dilute hydrogen in absolute units, as a function of energy transfer and at the two final energies of the experiment. At both energies, the calculated constant-θ spectra for 2° (circles) and 7° (stars) are shown. Error bars were estimated from the experimental uncertainties, including those related to the instrumental factor K_{YK} necessary to convert experimental intensities to double-differential cross-section data.

theoretical calculations, has thus provided important data for this fundamental system, while opening, at the same time, new possibilities for neutron data reduction to absolute units in inelastic scattering experiments, especially valuable at small angles, which we hope will be of

general help with the performance and analysis of accurate neutron measurements on new and existing instruments.

Acknowledgment

The authors wish to acknowledge the collaboration of Riccardo Messina (University of Palermo, Italy) during his INFM stage on neutron spectroscopy at the ILL.

References

[1] Balucani U and Zoppi M 1994 *Dynamics of the Liquid State* (Oxford: Clarendon)
[2] Marshall W and Lovesey S W 1971 *Theory of Thermal Neutron Scattering* (Oxford: Clarendon)
[3] Fermi E 1936 *Ric. Sci.* **7** 13
[4] Sachs R G and Teller E 1941 *Phys. Rev.* **60** 18
[5] Messiah A M L 1951 *Phys. Rev.* **84** 204
[6] Zemach A C and Glauber R J 1956 *Phys. Rev.* **101** 118
Zemach A C and Glauber R J 1956 *Phys. Rev.* **101** 129
[7] Krieger T J and Nelkin M S 1957 *Phys. Rev.* **106** 290
[8] Young J A and Koppel J U 1964 *Phys. Rev.* **135** A603
[9] Koppel J U and Young J A 1965 *Nukleonik* **8** 40
[10] Sears V F 1966 *Can. J. Phys.* **44** 1279
Sears V F 1966 *Can. J. Phys.* **44** 1299
[11] Lurie N A 1967 *J. Chem. Phys.* **46** 352
[12] Zoppi M 1993 *Physica* B **183** 235
[13] Guarini E 2003 *J. Phys.: Condens. Matter* **15** R775
[14] Egelstaff P A and Soper A K 1980 *Mol. Phys.* **40** 553
[15] Granada J R, Gillette V H, Pepe M E and Sbaffoni M M 2003 *J. Neutron. Res.* **11** 25
[16] Bafile U, Celli M and Zoppi M 1996 *Physica* B **226** 304
[17] Andreani C, Colognesi D, Filabozzi A, Pace E and Zoppi M 1998 *J. Phys.: Condens. Matter* **10** 7091
[18] Andreani C, Colognesi D and Pace E 1999 *Phys. Rev.* B **60** 10008
[19] Andreani C, Cipriani P, Colognesi D and Pace E 2000 *J. Phys.: Condens. Matter* **12** A139
[20] Celli M, Colognesi D and Zoppi M 2000 *Eur. Phys. J.* B **14** 239
[21] Herwig K W and Simmons R O 1992 *Mol. Phys.* **75** 1393
[22] Melkonian E 1949 *Phys. Rev.* **76** 1744
[23] Egelstaff P A and Schofield P 1962 *Nucl. Sci. Eng.* **12** 260
[24] Randolph P D, Brugger R M, Strong K A and Schmunk R E 1961 *Phys. Rev.* **124** 460
[25] Webb F J 1967 *Proc. Phys. Soc.* **92** 912
[26] Griffing G W 1961 *Phys. Rev.* **124** 1489
Griffing G W 1962 *Phys. Rev.* **127** 1179
[27] Guarini E, Casanova G, Bafile U and Barocchi F 1999 *Phys. Rev.* E **60** 6682
[28] Benmore C, Mos B, Egelstaff P and Verkerk P 1998 *J. Neutron. Res.* **6** 279
[29] Aisa D *et al* 2005 *Nucl. Instrum. Methods* A **544** 620
[30] Hansen J P and McDonald I R 1986 *Theory of Simple Liquids* (London: Academic)
[31] Herzberg G 1945 *Molecular Spectra and Molecular Structure* vol 2 (Princeton, NJ: van Nostrand-Reinhold)
[32] Michels A, De Graaf W, Wassenaar T, Levelt J M H and Louwerse P 1959 *Physica* **25** 25
[33] Fåk B, Alba M, Currat R and Brochier A 1991 Flux and calibration measurements on IN14 *Internal Report ILL91FA09T* Institut Laue-Langevin, Grenoble
[34] Paalman H H and Pings C J 1962 *J. Appl. Phys.* **33** 2635
[35] Petrillo C and Sacchetti F 1990 *Acta Crystallogr.* A **46** 440